2009, ApJ, 703, 285
Preprint typeset using LaTeX style emulateapj v. 04/20/08

arXiv:0904.1204v4 [astro-ph.CO] 28 Aug 2009

RADIO AND MID-INFRARED IDENTIFICATION OF BLAST SOURCE COUNTERPARTS IN THE CHANDRA DEEP FIELD SOUTH

Simon Dye[1], Peter A. R. Ade[1], James J. Bock[2], Edward L. Chapin[3], Mark J. Devlin[4], James S. Dunlop[5], Stephen A. Eales[1], Matthew Griffin[1], Joshua O. Gundersen[6], Mark Halpern[3], Peter C. Hargrave[1], David H. Hughes[7], Jeff Klein[4], Benjamin Magnelli[8], Gaelen Marsden[3], Philip Mauskopf[1], Lorenzo Moncelsi[1], Calvin B. Netterfield[9,10], Luca Olmi[11,12], Enzo Pascale[1], Guillaume Patanchon[13], Marie Rex[4], Douglas Scott[3], Christopher Semisch[4], Tom Targett[3], Nicholas Thomas[6], Matthew D. P. Truch[4], Carole Tucker[1], Gregory S. Tucker[14], Marco P. Viero[9] & Donald V. Wiebe[3]

2009, ApJ, 703, 285

ABSTRACT

We have identified radio and/or mid-infrared counterparts to 198 out of 350 sources detected at $\geq 5\sigma$ over ~ 9 deg^2 centered on the Chandra Deep Field South (CDFS) by the Balloon-borne Large Aperture Submillimeter Telescope (BLAST) at 250, 350 and 500 μm. We have matched 114 of these counterparts to optical sources with previously derived photometric redshifts and fitted SEDs to the BLAST fluxes and fluxes at 70 and 160 μm acquired with the Spitzer Space Telescope. In this way, we have constrained dust temperatures, total far-infrared/sub-millimeter luminosities and star formation rates for each source. Our findings show that on average, the BLAST sources lie at significantly lower redshifts and have significantly lower rest-frame dust temperatures compared to submm sources detected in surveys conducted at 850 μm. We demonstrate that an apparent increase in dust temperature with redshift in our sample arises as a result of selection effects. Finally, we provide the full multi-wavelength catalog of $\geq 5\sigma$ BLAST sources contained within the complete ~ 9 deg^2 survey area.

Subject headings: Submillimeter - surveys - cosmology: observations - galaxies: high-redshift - infrared: galaxies

1. INTRODUCTION

Excluding the cosmic microwave background, approximately half of the entire extragalactic background radiation is emitted at far infra-red (IR) and submillimeter (submm) wavelengths (e.g., Fixsen et al. 1998; Hauser & Dwek 2001) peaking around $\sim 200\mu$m. However, relatively little is known about the sources responsible compared to the well explored optical Universe where studies have enjoyed a head-start of several decades. Combining this with significant recent advances in submm instrumentation, it is therefore not surprising that galaxy surveys are now turning to the submm in the search for a more complete understanding of the formation of structure in the Universe.

The first deep submm surveys (e.g. Smail et al. 1997; Hughes et al. 1998; Barger et al. 1998) revealed a population of highly energetic dust obscured sources. Several clues suggested links between these systems and local ellipticals such as their similar volume densities (Scott et al. 2002; Dunne, Eales & Edmunds 2003) and clustering properties (e.g., Almaini et al. 2003; Blain et al. 2004) and their ability to rapidly form large stellar populations. Despite these early advances towards understanding the nature of the submm population, the small areal coverage common to the early surveys yielded a low number of sources, resulting in the usual limitations due to small number statistics and sampling variance. This motivated the largest and last of the surveys conducted using the Submillimeter Common User Bolometer Array (SCUBA; Holland et al. 1999), the SCUBA HAlf Degree Extragalactic Survey (SHADES; Mortier et al. 2005). SHADES detected a total of ~ 120 sources (down to $\sim 3.5\sigma$) at 850 μm over an area of ~ 700 arcmin^2 (Coppin et al. 2006).

Although the large homogeneous sample of submm sources detected by SHADES significantly enhanced previous samples, the survey still has three main deficits: 1) The areal coverage is small and therefore highly susceptible to sampling variance compared with optical surveys, 2) The SCUBA population appears to only represent a small fraction of the Universe's obscured star forma-

[1] Cardiff University, School of Physics & Astronomy, Queens Buildings, The Parade, Cardiff, CF24 3AA, U.K.
[2] Jet Propulsion Laboratory, Pasadena, CA 91109-8099, U.S.A.
[3] Department of Physics & Astronomy, University of British Columbia, 6224 Agricultural Road, Vancouver, BC V6T 1Z1, Canada
[4] Department of Physics & Astronomy, University of Pennsylvania, 209 South 33rd Street, Philadelphia, PA, 19104, U.S.A.
[5] Institute for Astronomy, University of Edinburgh, Royal Observatory, Edinburgh, EH9 3HJ, U.K.
[6] Department of Physics, University of Miami, 1320 Campo Sano Drive, Coral Gables, FL 33146, U.S.A.
[7] Instituto Nacional de Astrofísica Óptica y Electrónica (INAOE), Aptdo. Postal 51 y 72000 Puebla, Mexico
[8] Laboratoire AIM, CEA/DSM-CNRS-Université Paris Diderot, IRFU/Service d'Astrophysique, Bât. 709, CEA-Saclay, F-91191 Gif-sur-Yvette Cédex, France
[9] Department of Astronomy & Astrophysics, University of Toronto, 50 St. George Street Toronto, ON M5S 3H4, Canada
[10] Department of Physics, University of Toronto, 60 St. George Street, Toronto, ON M5S 1A7, Canada
[11] University of Puerto Rico, Rio Piedras Campus, Physics Dept., Box 23343, UPR station, Puerto Rico
[12] INAF, Osservatorio Astrofisico di Arcetri, Largo E. Fermi 5, I-50125, Firenze, Italy
[13] Université Paris Diderot, Laboratoire APC, 10, rue Alice Domon et Léonie Duquet 75205 Paris, France
[14] Department of Physics, Brown University, 182 Hope Street, Providence, RI 02912, U.S.A.

tion (see for example Chapman et al. 2005; Coppin et al. 2006; Dye et al. 2007). This is perhaps not surprising given that the energy of the far-IR/submm background at 850 μm is ~ 30 times less than at $\sim 200\mu$m where it peaks. 3) The SCUBA population seems to reside almost exclusively at redshifts $z \gtrsim 1$, preventing proper investigation of the link between distant dusty galaxies and the local population.

This paper is concerned with a large new submm survey centered on the Chandra Deep Field South (CDFS) recently carried out by the Balloon-borne Large Aperture Submillimeter Telescope (BLAST; Devlin et al. 2004; Pascale et al. 2008; Devlin et al. 2009). The survey covers $\sim 9\mathrm{deg}^2$ at each of the three BLAST wavelengths of 250, 350 and 500 μm. This is a leap of nearly two orders of magnitude in area compared with SHADES and energetically much nearer the peak of the far-IR/submm background.

BLAST bridges the gap between the longest wavelength channels available to the Spitzer Space Telescope (*Spitzer*) at 24, 70 and 160 μm and SCUBA at 850 μm. As we show in this paper, BLAST is substantially more sensitive to galaxies at $z \lesssim 1$ where SCUBA found very few sources yet maintains an overlap with SCUBA's sensitivity to moderate redshifts. For example, a 10 mJy 850 μm source at $z = 1$ with a dust temperature of 30 K has a typical flux of 80 mJy at 350 μm, well within the sensitivity levels reached by BLAST.

In order to derive scientific conclusions from the data in the same vein as for previous submm surveys, the first step is to identify counterparts to the sources detected by BLAST. Like all single dish submm observations made to date, the large beam size of BLAST precludes direct association with sources at optical to mid-IR wavelengths. A well proven procedure is to identify counterparts to submm sources using radio interferometry. At radio wavelengths, submm sources out to a redshift of ~ 3 can be readily detected. The typically low surface number density of radio detections results in a very low rate of chance alignments. In addition to radio counterparts, sources detected at 24 μm by *Spitzer* also prove useful for this purpose for the same reasons, albeit with typically lower positional accuracy (e.g. Ivison et al. 2007; Dye et al. 2008).

The main objective of this paper is to provide radio and 24 μm identifications of counterparts to the sources detected by BLAST in the CDFS. We have fitted spectral energy distributions (SEDs) to the three BLAST fluxes at 250, 350 and 500 μm and fluxes obtained by *Spitzer* at 70 and 160 μm. In this way, we have obtained best fit rest-frame dust temperatures, bolometric luminosities and star formation rates (SFRs). In Section 2 we describe the BLAST observations and the supporting multi-wavelength data used in our analyses. Section 3 outlines our methodology, in particular the procedure used for identifying counterparts in the radio and at 24 μm. The results are presented in Section 4. Finally, Section 5 summarizes our findings and briefly discusses the implications of our results.

The multi-wavelength catalog of $\geq 5\sigma$ BLAST sources is given in the appendix in Table 3 and contains 350 sources.

Throughout this work, we have assumed the following cosmology: $\Omega_m = 0.28$, $\Omega_\Lambda = 0.72$, $\mathrm{H}_0 = 70\ \mathrm{km\,s^{-1}}$.

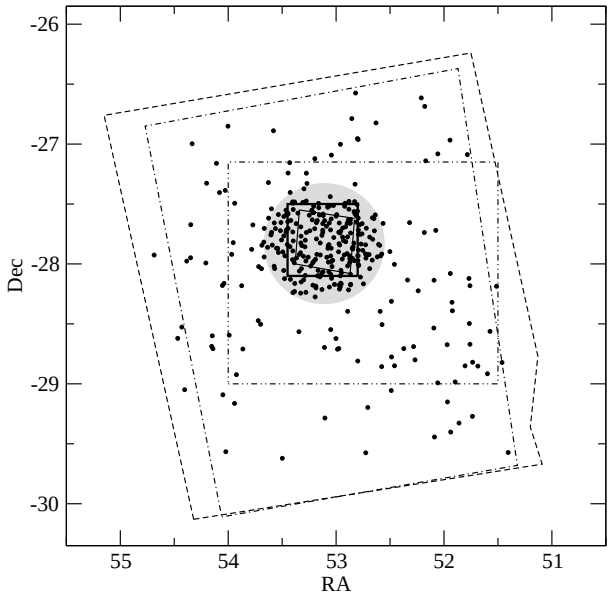

FIG. 1.— Geometry of the datasets used in this work: BLAST (BGS-Wide shown by the dashed line with BGS-Deep shaded gray), SWIRE 24 μm (dot-dash), Norris et al. radio catalog (dot-dot-dash), VLA CDFS radio data (thick continuous line) and the FIDEL 24 μm catalog (thin continuous line). The points show the $\geq 5\sigma$ BLAST sources.

2. DATA

Figure 1 plots the geometry of the various datasets used in this paper. This section gives details of those datasets and a brief description of the BLAST dataset itself. We refer the reader to Pascale et al. (2008) for a more detailed description of the primary characteristics of BLAST and Truch et al. (2008, 2009) for information on calibration and data reduction.

2.1. *BLAST Data*

The 250, 350 and 500 μm observations analyzed in this paper were acquired during the BLAST 2006 flight launched on the 21st of December from McMurdo Station, Antarctica (BLAST06). The data encompass the CDFS and cover $8.7\,\mathrm{deg}^2$ centered on ($3^\mathrm{h}32^\mathrm{m}$, $-28°12'$) with mean 5σ sensitivities of 180, 150 and 100 mJy/beam at 250, 350 and 500 μm respectively. A deep region of $0.8\,\mathrm{deg}^2$ is located within this $8.7\,\mathrm{deg}^2$, centered on the southern field of the Great Observatories Origins Deep Survey (GOODS; Dickinson et al. 2003) at ($3^\mathrm{h}32^\mathrm{m}30^\mathrm{s}$, $-27°48'$). This deeper region, referred to hereafter as 'BLAST GOODS South Deep' (BGS-Deep), reach mean 5σ sensitivities of 55, 45 and 30 mJy/beam at 250, 350 and 500 μm respectively (Devlin et al. 2009). The area surrounding BGS-Deep is referred to hereafter as BGS-Wide.

The BLAST time series data in each of the three bands were reduced using a custom-made pipeline (Pascale et al. 2008). Periodic observations of VY CMa conducted throughout the flight provide an absolute calibration for the telescope gain with uncertainties of 10%, 12% and 13% at 250, 350 and 500 μm respectively (although the calibration is highly correlated – see Truch et al. 2008). Signal and variance maps with $10'' \times 10''$ pixels were generated using the

maximum-likelihood map-making algorithm *SANEPIC* (Patanchon et al. 2008). In order to suppress residual large-scale noise, the *SANEPIC* maps were spatially filtered to whiten structure on scales larger than the telescope field of view ($14' \times 7'$). A catalog of point sources with a significance of $\geq 3\sigma$ for each band was compiled using a source-finding algorithm which selects the peaks in a smoothed map produced by the inverse variance weighted convolution of the image with the telescope point spread function (Devlin et al. 2009).

The source lists were synthesized into a common catalog using a procedure which accounts for the significance and positional uncertainty of the counterparts in each band. The radius of the 1σ positional error circle, σ_p, for a submm galaxy in a catalog with signal to noise μ which has not been corrected for Eddington bias can be expressed as

$$\sigma_p = 0.9\,\theta\,[\mu^2 - (2\alpha + 4)]^{-1/2} \quad (1)$$

for power-law counts of the form $n(> f) \propto f^{-\alpha}$, where θ is the full width at half maximum (FWHM) of the telescope beam (Ivison et al. 2007). The BLAST06 telescope beam is best fit by Gaussians with a FWHM of 36 arcsec, 42 arcsec and 60 arcsec at 250, 350 and 500 μm respectively (Pascale et al. 2008). Using this formula, error circles were calculated for each source in the individual catalogs assuming the slope of $\alpha = 2.5$ measured by Devlin et al. (2009). A minimum 1σ error circle of $5''$ was imposed, equal to the 1σ pointing uncertainty of the maps.

The combined catalog is comprised of all sources with a significance $\geq 5\sigma$ in at least one band. Sources from the other bands were considered counterparts if they were located within twice the radius of their respective error circles added in quadrature. Positions of sources in the resulting combined catalog were computed by averaging all the positions, weighted by σ_p^{-2}.

The catalog contains 350 sources in total as listed[1] in Table 3. The number of sources detected at $\geq 5\sigma$ by band is 178, 145 and 168 at 250, 350 and 500 μm respectively. 235 of the sources are located within BGS-Deep. Out of these, the sources detected at $\geq 5\sigma$ by band is 121, 113 and 124 at 250, 350 and 500 μm respectively.

2.2. *Radio Data*

We have used two different catalogs for our radio counterparts. The first contains sources detected in the 1.4GHz map observed by Miller et al. (2008) using the Very Large Array (VLA). The map covers an area of 0.33 deg^2 centered on the GOODS region to an average rms sensitivity of $\sim 8\mu$Jy per $2.8'' \times 1.6''$ beam. The published source catalog takes a very conservative detection threshold of 7σ. We therefore carried out our own source extraction on the map down to a lower detection threshold of 5σ. This results in a larger source surface number density of ~ 0.7 arcmin^{-2} compared to ~ 0.4 arcmin^{-2} in the originally published catalog. Although this increases the risk of introducing spurious sources, our Monte Carlo method of associating counterparts to the BLAST sources takes this into account.

[1] The BLAST data used in this paper (including maps) are also available for download at `http://blastexperiment.info`

For the second radio catalog, we used the shallower but wider 1.4GHz survey of (Norris et al. 2006) acquired using the Australia Telescope Compact Array. This survey covers a $\sim$ 4 deg^2 area ($2.2^\circ \times 1.8^\circ$) centered on ($3^{\rm h}31^{\rm m}$,$-28^\circ 06'$). The rms sensitivity of the survey is 40 μJy per $\sim 5''$ beam giving rise to a source number density of 0.05 arcmin^{-2}.

We carried out our identification of radio counterparts to the submm sources separately on each catalog. When matching to sources in the wider Norris et al. catalog, we excluded the region covered by the deeper VLA data. We verified that all of the Norris et al. sources in this region were contained within the VLA data.

2.3. *24 μm Data*

Similar to the radio data, our list of 24 μm *Spitzer* counterparts comprises two separate catalogs. The first is taken from Magnelli et al. (2009) as part of the Far-Infrared Deep Extragalactic Legacy Survey (FIDEL; Dickinson et al. 2007). The data cover 0.23 deg^2 ($30' \times 27'$) centered on the GOODS region. The 5σ point source sensitivity of FIDEL is $\sim 30\mu$Jy giving a source surface number density of 12 arcmin^{-2}.

The second 24 μm *Spitzer* catalog was taken from the Spitzer Wide-area InfraRed Extragalactic survey (SWIRE; Lonsdale et al. 2004) third data release[2]. The 24 μm SWIRE data in the CDFS cover $\sim$ 8 deg^2 ($2.4^\circ \times 3.4^\circ$) centered on ($3^{\rm h}32^{\rm m}$,$-28^\circ 15'$). The average 5σ point source sensitivity is $\sim 100\mu$Jy although only 24 μm sources detected at $\geq 15\sigma$ are included in the catalog.

In the same manner as our identification of radio counterparts, we identified 24 μm sources separately for both 24 μm catalogs excluding the deeper FIDEL region when searching for SWIRE counterparts. We verified that all 24 μm SWIRE sources are contained within the FIDEL data.

2.4. *70 & 160 μm Spitzer Maps*

In addition to the three BLAST fluxes, we also extracted flux from the SWIRE 70 and 160 μm *Spitzer* maps to improve constraints on our SED fitting. Both maps cover a rectangular area of $\sim 2.3^\circ \times 3.5^\circ$ centered on the 24 μm catalog ($3^{\rm h}32^{\rm m}$,$-28^\circ 15'$). All bar five of the $\geq 5\sigma$ BLAST sources with identified radio and/or 24 μm counterparts are located within these maps.

2.5. *Photometric redshifts*

For the purpose of fitting SEDs to the BLAST and *Spitzer* photometry, we matched identified counterparts to optical sources with previously estimated photometric redshifts. We used the two main photometric redshift catalogs publicly available in CDFS:

- The photometric redshift catalog of Wolf et al. (2004) from COMBO-17 (Classifying Objects by Medium-Band Observations in 17 filters) covers an area of 0.25 deg^2 ($0.5^\circ \times 0.5^\circ$) centered on GOODS. Redshifts are derived from optical photometry in five broad bands (U, B, V, R, I) and 12 interspersed medium bands. The surface number density of sources is 67 arcmin^{-2}. Redshifts extend up to $z \simeq 2$ and have a median of ~ 0.9.

[2] See http://irsa.ipac.caltech.edu/data/SPITZER/SWIRE

- The photometric redshift catalog of Rowan-Robinson et al. (2008) covers a total area of $\sim$ 5 deg^2 ($2.2^\circ \times 2.3^\circ$ but with gaps) centered on ($3^{\rm h}32^{\rm m}$,$-28^\circ30'$). The surface number density of sources is $\sim$ 9 arcmin^{-2}. Redshifts are estimated from SWIRE photometry: The five broad optical bands u, g, r, i and z and the two IRAC channels 3.6 and 4.5 μm. The median redshift is ~ 0.9 with 10% of galaxies at $z > 2$ and 4% at $z > 3$.

Table 1 lists the COMBO-17 and/or SWIRE photometric redshifts matched to the counterparts where available. Figure 5 shows the comparison for counterparts where both COMBO-17 and SWIRE redshifts exist.

3. METHODOLOGY

3.1. *Identification procedure*

To identify radio and 24 μm counterparts, we applied the frequentist technique of Lilly et al. (1999) based on the method of Downes et al. (1986). The method searches for objects close to the submm source and estimates the probability of each object being a chance alignment using a Monte Carlo approach. We applied the approach to the BLAST multi-wavelength source list described in Section 2.1 in the following way:

1) Select a random position within the area common to the BLAST and radio catalogs.

2) Find the minimum of the quantity $S = r_{sep}^2 n(> f)$ for each radio source within a separation cutoff of $20''$ of the random position (see below for justification of this cutoff). Here, r_{sep} is the radial separation between the radio source and the random position and $n(> f)$ is the surface number density of radio sources brighter than the radio source.

3) Repeat steps 1) and 2) for N realizations to determine the distribution of S for the radio sources.

4) Repeat steps 1) - 3) with the 24 μm catalog to determine the distribution of S for the 24 μm sources.

The distribution of S, $D(S)$, then allows the probability $P(< S_i)$ to be computed from a value S_i of a real potential counterpart i:

$$P(< S_i) = \frac{1}{N} \int_0^{S_i} D(S) dS \,. \qquad (2)$$

Note that, in general, up to a critical surface number density, $\int_0^\infty D\, dS < N$ since a certain fraction of the randomly chosen positions will not contain any radio (or 24 μm) sources within $20''$. Figure 2 shows the distributions obtained for radio and 24 μm counterparts in the FIDEL region.

The most likely counterpart is that with the lowest value of P. Introducing a threshold in P gives a criterion for establishing BLAST sources without counterparts. In the analysis that follows later in this paper, we have only included counterparts with $P \leq 0.05$. Sources with radio and 24 μm counterparts were included if either or both counterparts satisfy $P \leq 0.05$. Although not included in any analysis, we have also listed counterparts in the area outside the FIDEL region with $0.05 < P \leq 0.1$. As we discuss in Section 4.1, this is justified on the basis that relaxing the threshold to 0.1 results in another 29 counterparts at the mere cost of including an expected two additional false counterparts.

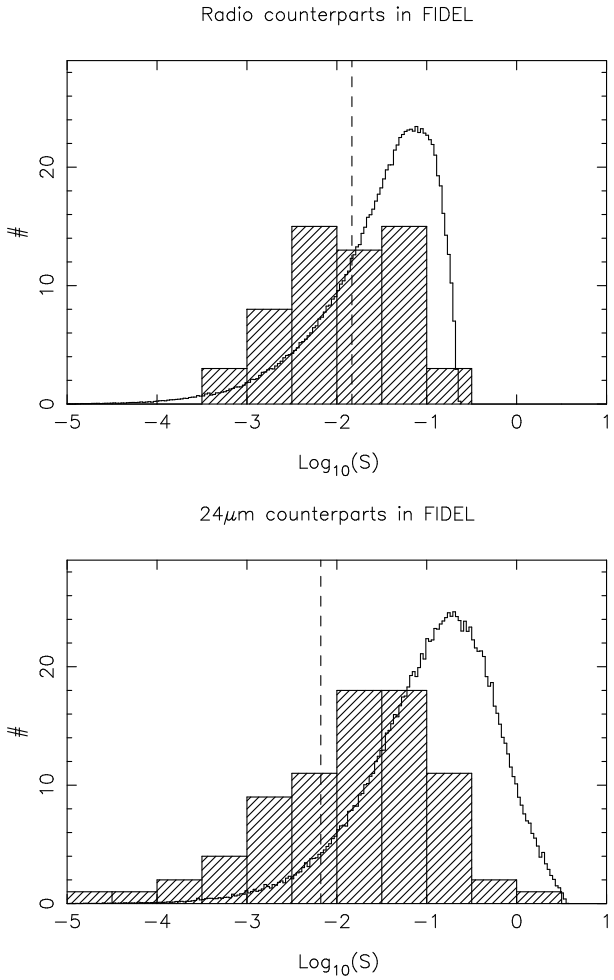

FIG. 2.— The distribution of $\log_{10}(S)$ for the radio and 24 μm data in the FIDEL region. The shaded histogram in each plot shows the distribution for the most likely counterparts lying within the separation cutoff of $20''$. The open histogram shows the distribution of lg(S) for one million randomly placed points (see text). The fact that the shaded histograms are skewed to lower S with respect to the open histograms indicates that a subset of the counterparts identified in the radio and at 24 μm genuinely trace the BLAST sources and are not completely unassociated (see Table 1). The dashed line corresponds to the threshold $P = 0.05$. (Note that this does not constrain 5% of the open histogram. Computation of P includes the random positions that do not contain any radio/24 μm sources which are not included in the histogram.)

3.1.1. *Determination of the separation cutoff*

Selection of the separation cutoff depends on several factors. Clearly a smaller cutoff gives rise to fewer counterparts, increasing the likelihood of missing a true counterpart. Conversely, a larger cutoff increases the risk of associating a very bright but unrelated counterpart (i.e., S is small since $n(> f)$ is small even though r_{sep} is large). An added complication is that larger cutoffs increase the probability of overlapping positional error circles thereby complicating the matching process.

The separation cutoff should be a compromise between these factors. We have therefore selected our cutoff as

the radius where the expected number of excluded true counterparts is equal to the expected number of false counterparts. The procedure we used to determine this is as follows:

- Using a large separation cutoff (e.g., 30″), perform an initial ID analysis as outlined above to compute values of P for all counterparts within the cutoff. Form the distribution of radial offsets of the primary counterparts (i.e., those counterparts with the lowest P per BLAST source).
- Compute the number of expected false IDs by summing P over all primary counterparts. Repeat the ID analysis with decreasing values of the separation cutoff, computing the expected number of false IDs each time. This gives the false ID rate, i.e., the number of false IDs per interval separation as a function of the separation cutoff.
- Subtract the false ID rate from the distribution of radial offsets determined in the first step. The result is the expected distribution of true counterparts which should have the form $r\,e^{-r^2/2\sigma^2}$ (e.g., Ivison et al. 2007). Fit this to derive σ and hence determine the number of true counterparts that would be excluded as a function of separation cutoff.

Figure 3 shows the distribution of radial offsets of the primary radio counterparts within 30″ of each BLAST source in the FIDEL region. The figure shows that the expected number of false counterparts is equal to the expected number of excluded true counterparts at a separation cutoff of 21″. Repeating this analysis for the 24 μm counterparts in the FIDEL region, we found an optimal separation cutoff of 19″. Similarly, the procedure returns optimal separation cutoffs of 28″ and 26″ for the radio and 24 μm counterparts in the region outside of FIDEL respectively. With this in mind, we chose a value of 20″ as the separation cutoff for the FIDEL region and 25″ for the region outside FIDEL. Whilst this is slightly conservative for the outer-FIDEL region, the fraction of real counterparts we would expect to exclude is low. Similarly, although this cutoff is slightly larger than the optimal value for the 24 μm counterparts within the FIDEL region, the false ID rate is sufficiently low around 20″ to make a negligible increase in the number of expected false 24 μm counterparts. Section 4.1 quantifies the resulting expected number of false IDs for each counterpart catalog and region.

Note that the distribution of radial offsets in Figure 3 indicates that 68% of radio counterparts are within an offset of $\sim 12''$. The position error of a 5σ BLAST source detected at 250 μm from equation 1 is $\sim 8''$. These values are consistent once positional uncertainties in the radio catalog and pointing errors on both the BLAST and radio catalogs are accounted for.

3.2. *Matching to the photometric catalogs*

Prior to matching to the photometric redshift catalogs, the identified radio counterparts were position-matched to the 24 μm counterparts. We used a separation tolerance of 3″ for this matching based on the 24 μm data

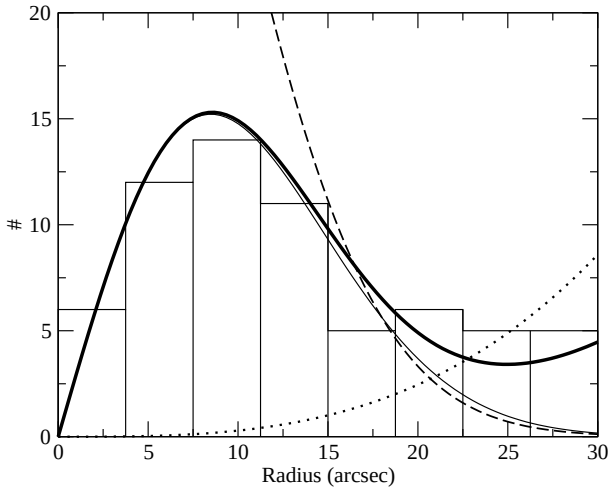

FIG. 3.— Distribution of radial offsets between BLAST sources and radio counterparts in the FIDEL region (open histogram). The dotted line shows the expected cumulative number of false radio IDs in this region as a function of the separation cutoff used in the matching. Subtracting the false ID rate (proportional to the gradient of the dotted line) from the histogram and fitting the result with a curve of the form $r\,e^{-r^2/2\sigma^2}$ gives the thin continuous line with $\sigma \simeq 8''$. The sum of this curve and the false ID rate gives the heavy continuous line which follows the histogram of measured radial offsets. Finally, the dashed curve shows the cumulative number of true radio counterparts that would be excluded at the given separation cutoff. The optimal separation cutoff is selected as the radius where the expected number of false IDs is equal to the expected number of excluded true counterparts. In this case, for the radio counterparts in FIDEL, the optimal cutoff is 21″.

point spread function (PSF) of FWHM $\simeq 6''$ and the average radio data PSF of FWHM $\simeq 5''$. In cases where a BLAST source has a radio and a 24 μm counterpart that both satisfy the selection criteria but are separated from each other by more than 3″, we selected the counterpart with the lowest value of P.

All identified BLAST source counterparts were then position-matched to the photometric redshift catalogs. For BLAST sources with a radio and a 24 μm counterpart, the average of the radio and 24 μm co-ordinates were used in the matching (since the radio and 24 μm PSFs are similar). We used the same positional tolerance of 3″ in matching up with the redshift catalogs. We found that in all cases where a counterpart is matched by both a COMBO-17 and SWIRE redshift (i.e., they are both within 3″ of the counterpart), the COMBO-17 and SWIRE sources are within 1″ of each other.

3.3. *SED fitting*

We determined 250, 350 and 500 μm BLAST fluxes and the 70 and 160 μm *Spitzer* fluxes for the BLAST sources with identified photometric redshifts by reading off the flux in the beam-convolved maps at the position of the radio/24 μm counterpart. These fluxes were then fitted with a modified black body SED of the form $A\nu^{\beta}\mathrm{B}(\nu,\mathrm{T})$, where A is a normalization constant, B is the Planck function and β was fixed[3] at the value of 1.5.

In fitting the SEDs, we assumed a uniform prior for the temperature over 10 K$\leq T \leq$50 K and fixed the redshift

[3] Allowing β to vary in the minimization generally results in an improvement in χ^2 of less than 1, implying that the data do not support the introduction of an extra parameter. This was also found to be true when a secondary dust component was added.

at the photometric redshift of the optical counterpart. In cases where a redshift exists from both COMBO-17 and the catalog of Rowan-Robinson et al. (2008), we selected the redshift that minimizes χ^2 which was computed allowing for the BLAST data covariance (see Truch et al. 2008):

$$\chi^2 = \sum_{i,j}(f_i - f_i^m(\beta,T,z))\sigma_{ij}^{-1}(f_j - f_j^m(\beta,T,z)) + \sum_k (f_k - f_k^m(\beta,T,z))^2/\sigma_k^2 \quad (3)$$

where the subscripts i and j span the three BLAST bands and the subscript k spans the 70 and 160 μm *Spitzer* bands. In this equation, σ_{ij}^{-1} is the inverse of the BLAST data covariance matrix, σ_k is the error on the kth *Spitzer* flux, f_i is the flux measured in the ith band and f_i^m is the corresponding model flux computed by integrating the trial SED over the ith band response function. The total far-IR/submm luminosities quoted in the results that follow were computed by integrating the best fit SED over the wavelength range 10 - 2000 μm.

We have ignored the effects of flux boosting on the properties derived from the SED fits. In reality, since the BLAST differential source count density falls very rapidly with flux (approximately following $\mathrm{d}N/\mathrm{d}S \propto S^{-3.5}$ – see Patanchon et al. 2009), the effects of Eddington bias and source confusion mean that the fluxes in our source catalog are slightly boosted. However, by restricting our analysis to a relatively bright subset of the BLAST source catalog and also extracting flux densities at the radio or MIPS source positions, we expect any boosting to be manageable. In fact, repeating our analysis on a preliminary de-boosted dataset indicates a small flux bias which results in a small scatter with negligible bias to the derived far-IR luminosities and a slight bias of approximately +2K to the dust temperatures. A full treatment of flux boosting in the BLAST data will be explored in future work.

4. RESULTS

Several of the results presented in this section, where stated, are limited to a robust sample of sources. We have defined this robust sample based on the results of the SED fitting discussed below. The robust sample is therefore a subset of those sources with photometric redshifts.

A source is considered robust if its best fit rest-frame dust temperature is not at the extremes of our uniform temperature prior (i.e., if 10K $< T <$ 50K) and if its SED can be fit with $\chi^2 \leq N_{dof} + 2.71$, where N_{dof} is the number of degrees of freedom of the fit. For normally distributed errors, this threshold in χ^2 corresponds to excluding the worst fit 10% of SEDs. For almost all of our sources, $N_{dof} = 3$ since we have five flux measurements and two SED parameters (normalization and T). With these criteria, our robust sample contains 74 BLAST sources.

Defining the robust sample in terms of the SED fitting is motivated by the fact that source redshifts are fixed at the value of the photometric redshift estimated for the counterpart. If the assumed redshift is incorrect, either because the photometric redshift is intrinsically unreliable or because the BLAST source has been spuriously identified with the counterpart, then this will manifest itself either with a poor SED fit or by requiring an extreme temperature to obtain an acceptable fit.

4.1. *Identifications*

Table 1 lists the BLAST sources within the FIDEL region with identified radio and/or 24 μm counterparts. Table 2 lists the radio and 24 μm counterparts to the $\geq 5\sigma$ BLAST sources located outside the FIDEL region.

Within the FIDEL region the 24 μm identification rate ($P \leq 0.05$) is 23/78 compared with the radio identification rate of the VLA data of 29/78. The overall identification rate, i.e., a BLAST source being identified with $P \leq 0.05$ by either a radio or 24 μm source is 39/78 in the FIDEL area. Splitting this by band, the overall rates (as a fraction of sources detected at $\geq 5\sigma$ at each wavelength) are 31/42 at 250 μm, 26/45 at 350 μm and 16/48 at 500 μm. In the area outside the FIDEL region, the 24 μm identification rate of the SWIRE data is 131/268 compared with the rate of the Norris et al. data (and the outer part of the VLA data) of 74/220.

Figure 6 plots the overall identification rate as a function of 250 and 500 μm flux for sources detected at $\geq 5\sigma$ at each wavelength. The figure shows a small decline in the identification rate of BLAST sources towards fainter 250 μm fluxes and a stronger decline towards fainter 500 μm fluxes. Over the full area common to the radio and 24 μm data, this decline corresponds to 37 out of 150 of the 250 μm sources not being identified and 94 out of 146 of the 500 μm sources not being identified. Despite benefitting from a negative K-correction (which is quite weak at 250 μm), lower flux BLAST sources are more likely to reside at higher redshifts. The measured decrease in identification rate at lower fluxes therefore implies firstly that the unidentified sources lie at higher redshifts than the identified sources on average and secondly that there is a larger fraction of unidentified high redshift 500 μm sources. Section 4.2.1 discusses this further.

By summing the values of P determined in the identification process, the number of expected false counterparts in the sample can be estimated. Out of all 103 radio counterparts identified with $P_r < 0.05$, ~ 1 of these is expected to be false. Similarly, out of all 154 24 μm sources with $P_{24} < 0.05$, ~ 2 counterparts would be expected to be false. Limiting this to our robust sample of counterparts, the expected number of false identifications is ~ 1 out of 46 in the radio and ~ 1 out of 56 at 24 μm.

Relaxing the threshold on P to 0.1 in the area outside the FIDEL region results in an additional 29 counterparts. Summing P over these 29 counterparts indicates that two of them would be expected to be chance alignments. On this basis, we have included counterparts up to $P \leq 0.1$ in Table 2. However, these additional sources are only listed in the table and are not included in any analysis in this paper.

4.2. *Redshifts*

Figure 4 shows the distribution of redshifts for our robust sample of 74 BLAST sources. The figure also shows the redshift distribution of the SCUBA sources detected at 850 μm by Chapman et al. (2005) and Aretxaga et al. (2007). The submm sources in our robust sample are

TABLE 1
Radio and 24 μm counterparts to the $\geq 5\sigma$ BLAST sources in the FIDEL region

ID	α (radio)	δ (radio)	$f_{\rm r}$	$P_{\rm r}$	$d_{\rm r}$	α (24 μm)	δ (24 μm)	f_{24}	P_{24}	d_{24}	$z_{\rm RR}$	z_{17}	T	$L_{\rm FIR}$	χ^2
4	53.14622	-27.92569	0.06	0.0082	1.9	53.14611	-27.92573	5.150	0.0006	2.0	0.06	0.04	$23.3^{+1.2}_{-1.2}$	1.47	13.6
6	53.12452	-27.74028	0.34	0.0242	10.4	53.12444	-27.74005	6.930	0.0022	9.5	0.05	0.07	$25.8^{+0.8}_{-0.8}$	2.58	1.99
7	53.20818	-27.57581	0.31	0.0361	12.7	-	-	-	-	-	-	0.23	$26.2^{+1.6}_{-1.2}$	20.8	12.9
17	53.20553	-27.97914	0.21	0.0177	6.5	53.20553	-27.97916	0.333	0.1036	6.6	-	1.23	$34.6^{+2.4}_{-2.0}$	399.	4.79
22	52.96724	-27.65742	0.99	0.0158	11.0	52.96697	-27.65738	0.424	0.1808	11.9	-	0.39	$16.1^{+1.6}_{-1.2}$	16.0	3.68
23	53.24674	-27.72369	0.16	0.0479	11.1	53.24668	-27.72363	0.324	0.2288	10.9	-	1.12	$29.8^{+3.2}_{-2.8}$	241.	1.70
24	52.87452	-27.95632	0.15	0.0196	5.9	52.87456	-27.95623	0.275	0.1184	5.9	-	-	-	-	-
26	53.19183	-27.96262	0.07	0.0083	2.1	53.19150	-27.96259	2.420	0.0012	2.0	-	0.11	$23.3^{+1.6}_{-1.6}$	2.47	0.56
34	52.95710	-27.72408	0.15	0.0332	8.5	52.95720	-27.72392	1.040	0.0357	9.0	0.47	0.56	$22.1^{+2.0}_{-2.0}$	41.3	2.16
35	53.07106	-27.97958	3.04	0.0228	19.0	53.07101	-27.97958	0.064	0.8407	19.0	-	1.17	$32.2^{+3.6}_{-3.2}$	256.	3.93
36	53.32402	-27.76846	0.11	0.0081	2.9	53.32407	-27.76831	0.471	0.0152	2.9	-	1.56	$29.4^{+2.4}_{-2.0}$	461.	1.39
42	52.93913	-27.77780	0.06	0.0387	5.0	52.93900	-27.77783	0.308	0.0811	5.3	-	0.95	$33.0^{+3.6}_{-3.6}$	127.	11.1
43	53.29048	-27.80045	0.34	0.0628	19.7	53.29046	-27.80044	2.590	0.0497	19.6	-	0.16	$28.2^{+1.6}_{-2.0}$	5.82	13.2
54	-	-	-	-	-	52.96448	-27.74109	0.081	0.0414	1.4	-	0.94	$24.1^{+2.4}_{-2.4}$	127.	1.15
55	52.87458	-27.93354	0.14	0.0094	3.7	-	-	-	-	-	-	1.83	$47.6^{+2.4}_{-5.7}$	952.	20.1
63	53.31882	-27.84430	0.11	0.0256	6.0	53.31881	-27.84427	3.590	0.0037	6.1	-	0.11	$27.0^{+1.2}_{-1.2}$	2.51	7.00
66	53.02044	-27.77983	0.09	0.0138	3.5	53.02031	-27.77980	0.591	0.0186	3.9	-	1.16	$30.2^{+3.2}_{-2.8}$	229.	3.89
68	52.94418	-27.95975	0.41	0.0054	4.4	52.94399	-27.95965	1.250	0.0056	3.7	0.26	0.36	$32.6^{+2.0}_{-1.6}$	40.9	1.74
85	-	-	-	-	-	52.97289	-27.83057	0.032	0.0119	0.5	1.07	0.73	$19.3^{+2.0}_{-2.0}$	59.0	2.81
102	52.85398	-27.86892	12.79	0.0040	10.7	52.85364	-27.86877	0.381	0.1525	9.6	1.28	1.18	$41.9^{+4.4}_{-4.4}$	357.	2.80
110	53.07441	-27.84972	0.05	0.0725	7.6	53.07444	-27.84973	1.140	0.0229	7.7	0.43	0.12	$23.3^{+2.4}_{-2.4}$	1.90	0.68
112	53.17499	-27.63874	29.46	$< 10^{-4}$	2.3	-	-	-	-	-	-	0.83	$31.8^{+6.1}_{-4.4}$	98.9	5.68
125	53.12247	-27.58556	0.08	0.0338	5.7	-	-	-	-	-	1.14	0.43	$41.1^{+4.4}_{-4.8}$	259.	10.5
131	53.00352	-27.59926	2.03	0.0139	13.4	-	-	-	-	-	0.99	0.92	$25.4^{+4.8}_{-4.4}$	102.	10.0
132	53.10444	-27.63972	0.11	0.0374	7.9	53.10435	-27.63956	0.432	0.0943	7.8	-	0.62	$22.5^{+3.2}_{-2.8}$	38.9	0.78
136	53.11902	-27.59375	0.09	0.0717	10.4	53.11897	-27.59353	1.080	0.0462	11.2	0.56	0.69	$28.6^{+3.6}_{-3.6}$	74.6	0.20
145	-	-	-	-	-	53.04655	-27.98295	1.380	0.0081	5.0	0.25	0.23	$20.9^{+2.8}_{-2.4}$	7.00	3.25
162	52.97921	-27.73632	0.28	0.0356	11.8	52.97908	-27.73624	0.131	0.5468	11.3	0.77	1.22	$32.6^{+4.4}_{-4.0}$	207.	0.20
167	53.19950	-27.70914	0.19	0.0427	11.4	53.19949	-27.70913	1.070	0.0486	11.3	-	0.98	$21.3^{+2.8}_{-2.4}$	84.5	2.19
174	-	-	-	-	-	53.12323	-27.66337	0.021	0.0248	0.6	-	0.95	$32.2^{+6.9}_{-6.1}$	65.0	15.1
179	53.24705	-27.59286	0.19	0.0154	5.6	53.24717	-27.59282	0.557	0.0338	5.3	-	1.12	$30.6^{+5.3}_{-4.0}$	111.	8.22
198	53.06759	-27.65860	0.08	0.0913	12.4	53.06747	-27.65842	1.490	0.0326	12.0	0.37	1.34	$22.1^{+4.4}_{-3.6}$	11.9	3.17
218	52.92426	-27.92695	0.10	0.0323	6.7	52.92403	-27.92716	0.191	0.2590	7.5	-	0.91	$25.4^{+3.2}_{-2.8}$	86.0	3.07
221	53.04864	-27.62401	4.05	0.0048	9.0	53.04847	-27.62387	1.830	0.0181	8.7	-	1.55	$24.5^{+4.0}_{-3.2}$	196.	4.32
235	53.26131	-27.94520	0.27	0.0367	11.8	53.26065	-27.94578	0.204	0.4137	11.7	-	-	-	-	-
240	-	-	-	-	-	53.27565	-27.73757	0.327	0.0019	0.6	-	0.84	$30.6^{+4.8}_{-4.0}$	102.	3.49
250	52.91480	-27.68874	0.20	0.0319	9.4	52.91470	-27.68874	1.460	0.0215	9.1	0.94	2.09	$24.9^{+4.0}_{-3.6}$	75.3	1.73
262	53.18002	-27.92068	0.07	0.0373	5.9	53.17995	-27.92065	0.539	0.0388	5.7	-	1.32	$26.6^{+3.2}_{-3.2}$	150.	3.37
265	-	-	-	-	-	52.86584	-27.74164	0.048	0.0096	0.5	-	-	-	-	-

Note. — (see Table 2 for the counterparts outside FIDEL). Reading from the left, columns are: radio co-ordinates, radio flux, f_r/mJy, probability of radio counterpart being a chance alignment, P_r, radio radial offset, $d_{\rm r}$/arcsec, 24 μm co-ordinates, 24 μm flux, f_{24}/mJy, probability of 24 μm counterpart being a chance alignment, P_{24}, 24 μm radial offset, d_{24}/arcsec, photometric redshift from Rowan-Robinson et al., $z_{\rm RR}$, COMBO-17 photometric redshift, z_{17}, best fit temperature, T/K, total far-IR/submm luminosity, $L_{\rm FIR}/(10^{10}L_{\odot})$ and χ^2 of the SED fit.

clearly located at significantly lower redshifts than those detected by SCUBA. The median redshift of the sample of 73 SCUBA sources of Chapman et al. (2005) lies at $z = 2.2$ with an inter-quartile range of $1.7 - 2.8$ and the sample of 120 SCUBA sources of Aretxaga et al. (2007) has a median of $z = 2.4$ and inter-quartile range of $1.8 - 3.1$. In comparison, the distribution of redshifts of our robust sample has a median of ~ 0.6 and an inter-quartile range of $0.2 - 1.0$.

Figure 5 shows a comparison of the optical photometric redshifts for all sources that have a redshift provided by both Rowan-Robinson et al. (2008) and COMBO-17. The agreement is mediocre with a third of the 21 redshifts inconsistent at the $> 3\sigma$ level (although without uncertainties on the Rowan-Robinson redshifts the number of inconsistencies quoted here is an upper limit). However, in fitting the SEDs, for cases where both a Rowan-Robinson and COMBO-17 redshift exists, we took the redshift which gives the best fit to the submm/far-IR data. Furthermore, by limiting our analysis of the derived source properties to the robust sample, the majority of inaccurate photometric redshifts will be ruled out.

We also very recently obtained spectroscopic redshifts

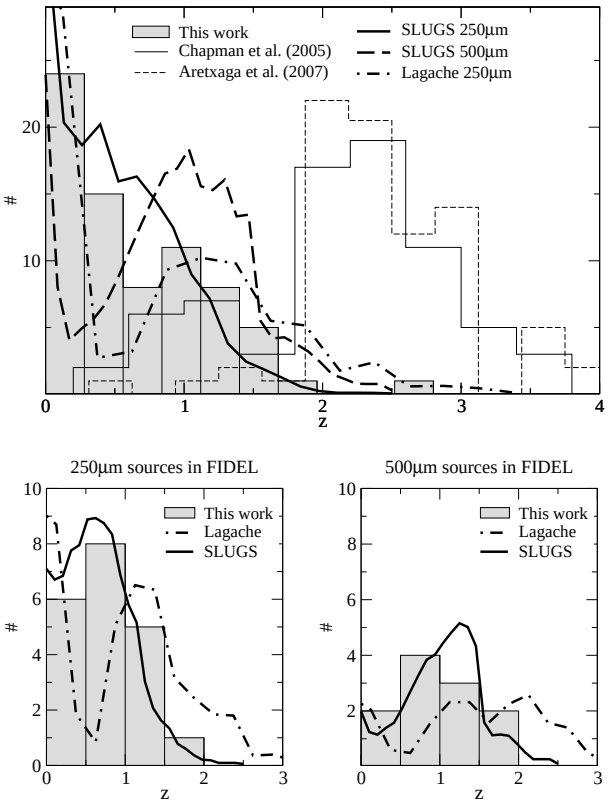

FIG. 4.— *Top panel*: The shaded histogram shows the distribution of photometric redshifts for the 74 BLAST sources in our robust sample. Where a counterpart has a redshift estimate from both COMBO-17 and the catalog of Rowan-Robinson et al. (2008), the redshift that gives the best modified black body SED fit to the BLAST and *Spitzer* flux is taken. The two open histograms with the thin continuous and dashed lines respectively show the distribution of submm sources detected at 850 μm by Chapman et al. (2005) and Aretxaga et al. (2007). The thick continuous and thick dashed lines show the predicted redshift distribution for 250 μm sources and 500 μm sources respectively, computed by evolving the SLUGS local 850 μm luminosity function of Dunne et al. (2000) using the model of Rowan-Robinson et al. (2001). *Bottom left panel*: The redshift distribution of robust sources detected at 250 μm in the FIDEL region (shaded histogram). Over-plotted is the distribution of 250 μm sources predicted by our evolved SLUGS model (continuous line) and by the models of Lagache et al. (2004, dot-dashed line). *Bottom right panel*: The same as the bottom left panel but for robust 500 μm sources in the FIDEL region.

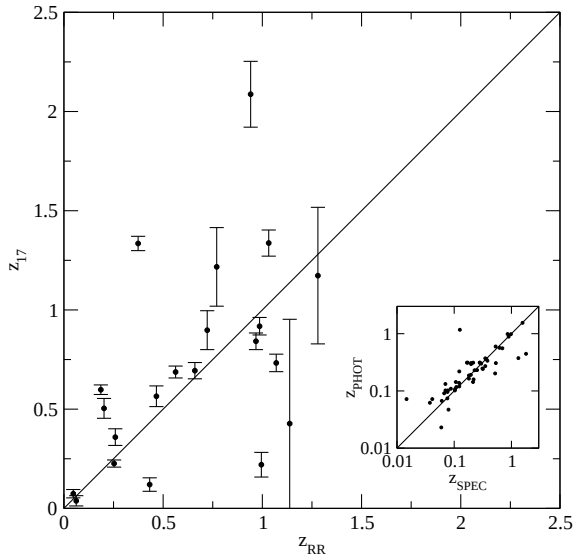

FIG. 5.— *Main panel*: Comparison of Rowan-Robinson et al. (2008) and COMBO-17 photometric redshifts for 21 of the $\geq 5\sigma$ BLAST sources where both redshifts are available. *Inset panel*: Comparison of our recently obtained spectroscopic redshifts (Eales et al. 2009) with the 53 photometric redshifts in common with the current work. Where two photometric redshifts exist for a given source, we have taken that which gives the best SED fit to the observed submm/far-IR data. Only three out of the 53 photometric redshifts are discrepant with the spectroscopic redshifts at the $> 2\sigma$ level.

for approximately half of our radio and/or 24 μm identified $\geq 5\sigma$ BLAST sources (Eales et al. 2009). Preliminary analysis has indicated excellent agreement with the photometric redshifts we have used in the current work. The inset panel in Figure 5 shows this comparison for the 53 sources in common and indicates that our method of selecting the photometric redshift that best fits the observed fluxes when two redshifts are available works well. Although we have not incorporated the spectroscopic redshifts in the analysis carried out in this paper, this excellent agreement increases the confidence in the source properties that follow from the SED fitting, since these strongly depend on the redshift assumed.

4.2.1. *Comparison with model predictions*

We have predicted the redshift distribution of the BLAST sources using an empirical model (Eales et al. 2009) derived from the results of the SCUBA Local Universe and Galaxy Survey (SLUGS; Dunne et al. 2000; Vlahakis et al. 2005). The model is based on the sample of 104 galaxies observed by Dunne et al. (2000) using SCUBA at 450 and 850 μm. The galaxies form a statistically-complete sample above a 60μm flux limit of 5.24 Jy and constitute the only large sample of galaxies with empirical spectral energy distributions that stretch from the far-IR to submm wavebands, which is a major advantage over existing models for submm surveys.

We can use the SLUGS sample to predict the source counts at any frequency in a straightforward way. The number of sources above a given 250 μm flux density is given by

$$N(> f_{250}) = \sum_{j=1}^{104} \int_0^{z(L_j(z),f_{250})} \frac{1}{V_j}\, dV \qquad (4)$$

where V_j is the comoving volume in which the jth SLUGS source could have been detected in the original sample from which it was selected, and the integral is over comoving volume out to the redshift at which the source would be detected in the current sample. We assumed that the luminosity of the jth SLUGS galaxy is given by

$$L_j(z) = E(z)L_j(0) \qquad (5)$$

where $L_j(0)$ is the empirical luminosity of the jth SLUGS galaxy at the appropriate rest-frame wavelength and $E(z)$ is an evolution function. We have implicitly assumed 'luminosity evolution' rather than 'number-density evolution', which is necessary anyway because it is impossible to fit both the cosmic background radiation and the submm source counts with number-density evolution. In practice, we have used the simple luminosity-evolution model from Rowan-Robinson et al. (2001), in

which luminosity is given by

$$L(t) = L(t_0)\left(\frac{t}{t_0}\right)^D \exp\left[C\left(1 - t/t_0\right)\right] \qquad (6)$$

where t is the time from the big bang and t_0 is the time at the current epoch. C and D are parameters of the model. We have found that values of $C = 9$ and $D = 3$ give acceptable fits to the spectral shape and intensity of the cosmic background radiation and to the SCUBA 850 μm and *Spitzer* 70 μm source counts. By adjusting the integral limits in equation (4), the distribution of redshifts can be computed.

The predicted redshift distribution for the BLAST galaxies detected at $\geq 5\sigma$ at 250 μm and at 500 μm using this approach is shown in the top panel of Figure 4. In addition, the figure shows the redshift distribution according to the galaxy evolution model of Lagache et al. (2004). The predictions apply specifically to the BLAST CDFS survey, taking into account the different areas and depths of BGS-Wide and BGS-Deep.

To allow for possible biases in our BLAST catalogue caused by flux boosting and source confusion, we have disregarded absolute model normalizations throughout this section and have instead normalized the model counts to match the BLAST counts. In this way, our aim is to compare only distribution morphologies. We refer the reader to Patanchon et al. (2009) for an account of the BLAST number counts and the subsequent implications for models.

A more direct comparison of the model redshift distributions is shown in the bottom two panels of Figure 4. Here, we have limited the comparison to the FIDEL area where the BLAST, radio and 24 μm data are deepest and most uniform. The bottom left panel shows the redshift distribution of the 20 robust sources detected at 250 μm. Similarly, the bottom right panel shows the redshift distribution of the 11 robust sources detected at 500 μm. Both lower panels show the corresponding distributions predicted by our evolved SLUGS model and the Lagache et al. model.

The Lagache et al. and evolved SLUGS model distributions show considerable differences. In the 250 μm case, the largest discrepancy occurs at $z < 1$. The Lagache et al. model predicts a deficit around $z \simeq 0.5$ at the division between the quiescent population at $z < 0.5$ and the starbursting population at $z > 0.5$. However, according to the evolved SLUGS model, a peak is anticipated at $z \simeq 0.5$. The measured distribution more closely resembles the SLUGS model although the large uncertainty due to Poisson noise means that the data can not be used to unambiguously validate one model over the other. In the case of the 500 μm sources, there are similar discrepancies between the models. Once again, the evolved SLUGS model appears more consistent with the observed redshifts but the dominant Poisson noise precludes verification of either model.

Despite their differences, neither of the model redshift distributions in Figure 4 implies that we have failed to identify counterparts or obtain redshifts for a significant number of $\geq 5\sigma$ sources beyond $z \simeq 2$ where $> 80\%$ of the SCUBA population resides. Of the two models considered, the Lagache et al. model is most discrepant with our sample, implying that we may have missed a small

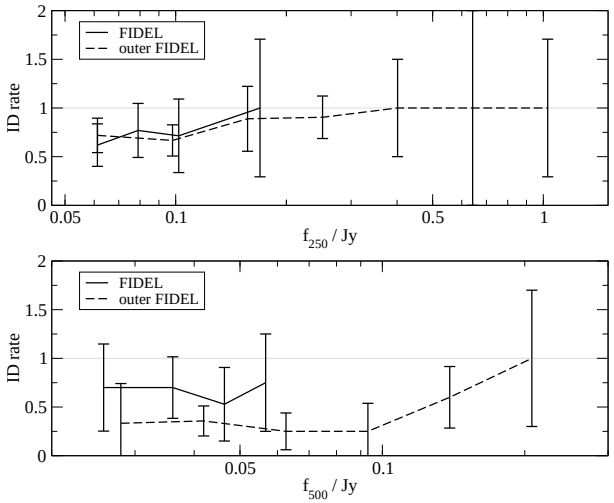

FIG. 6.— The identification rate of BLAST sources (having either a radio or 24 μm counterpart) as a function of 250 μm flux (top) and 500 μm flux (bottom). In both plots, the continuous line corresponds to the FIDEL region and the dashed line to the area outside FIDEL common to the radio and 24 μm data. The plots include only those sources detected with significance $\geq 5\sigma$ at each wavelength.

fraction of higher redshift sources. This is indeed consistent with our expectations based on the declining identification rate of 250 μm sources toward fainter fluxes (see Figure 6). However, neither the Lagache et al. model nor the SCUBA model predicts a sufficient fraction of high redshift 500 μm sources required to explain the stronger decline in identification rate seen at fainter 500 μm fluxes.

A obvious question that arises is to what degree does the fraction of sources without redshifts reconcile the differences between the SCUBA redshift distributions mentioned previously and the redshift distribution of our robust sample? Would we expect some of these sources to coincide with the SCUBA population? Unfortunately, we can only provide an upper limit. Figure 7 plots the radio flux versus the 24 μm flux for all counterparts identified at both wavelengths. Sources in the robust sample (which all have photometric redshifts) are indicated by filled points. The distribution of non-robust sources (mostly without redshifts) is clearly not concentrated in any specific part of the $f_r - f_{24}$ plane, in particular at faint fluxes where more distant sources would be expected to lie. (Although not shown, the same is true when every source with a redshift is over-plotted). The rate of assignment of redshifts within the sub-sample of BLAST sources with counterparts therefore does not decline at higher redshifts at a detectable level. This in turn means that if we had been able to obtain redshifts for all 198 identified counterparts, their redshift distribution would be similar in shape to that of our robust sample except with greater normalization. Therefore, even under the extreme assumption that all 153 unidentified sources lie at high redshift ($z \gtrsim 2$), there is still only an overlap of just under 50% with the SCUBA population.

However, we emphasize that the $\geq 5\sigma$ sources considered in this paper are at the bright end of the sources detected by BLAST within BGS-Deep/Wide. The fainter sources, generally detected with lower significance, are expected to probe higher redshifts. This does indeed seem to be borne out by the detection of a signifi-

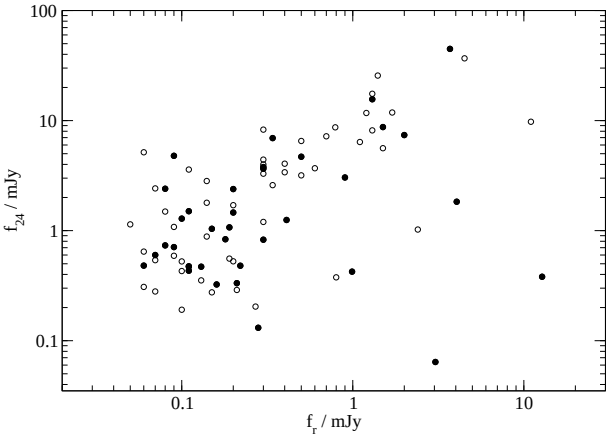

FIG. 7.— Correlation between 1.4GHz radio flux and 24 μm *Spitzer* flux for all counterparts to the $\geq 5\sigma$ BLAST sources identified at both wavelengths. The filled symbols denote sources in the robust sample (all of which have photometric redshifts).

cant fraction of the extragalactic far-IR/submm background from fainter, higher redshift BLAST sources (Pascale et al. 2009; Marsden et al. 2009).

4.3. *Source SEDs*

Tables 1 and 2 list the best fit rest-frame dust temperatures and total far-IR/submm luminosities for the 114 sources with available photometric redshifts. The SEDs for those sources located in the FIDEL region are plotted in Appendix A.

In Figure 8 we plot the total far-IR/submm luminosity, $L_{\rm FIR}$, of the BLAST sources in the robust sample against redshift. Superimposed on this plot are curves showing the minimum $L_{\rm FIR}$ a source must have in order to be detected at 5σ in one of the three BLAST bands. These thresholds were computed using the survey sensitivity in BGS-Deep (55, 45 and 30 mJy/beam at 250, 350 and 500 μm respectively to 5σ) hence sources in the shallower region will be subjected to a set of curves shifted to slightly lower redshifts. The band in which the detection limit occurs varies as a function of redshift and dust temperature (e.g., a 10 K source meeting the requirement for a detection of 5σ in one of the three bands will only ever be met in the 500 μm band). The figure shows that for a given $L_{\rm FIR}$ out to a redshift of $z \simeq 1.6$, cooler sources can be detected at greater distances. Beyond this redshift, 10 K sources begin to rapidly move out of the 500 μm band and increasingly warmer sources become more readily detected. However, since the curves for hotter sources (40-50 K) become flatter at higher redshifts, a small increase in temperature of a hotter source pushes the detection limit to much lower redshifts. The net result is that there exists a modal mid-range dust temperature that slowly rises with redshift.

A complication is that the above argument assumes the sources have a uniform distribution of dust mass. In practice, a cooler source at high redshift must have substantially more dust than a hotter source to remain detected. Since sources with more dust are more rare, this greatly reduces the probability of detecting cooler sources (10-20 K) out to higher redshifts ($z \gtrsim 1.5$). We return to this point below.

Figure 9 shows the distribution of best fit rest-frame dust temperatures in our robust sample for the assumed

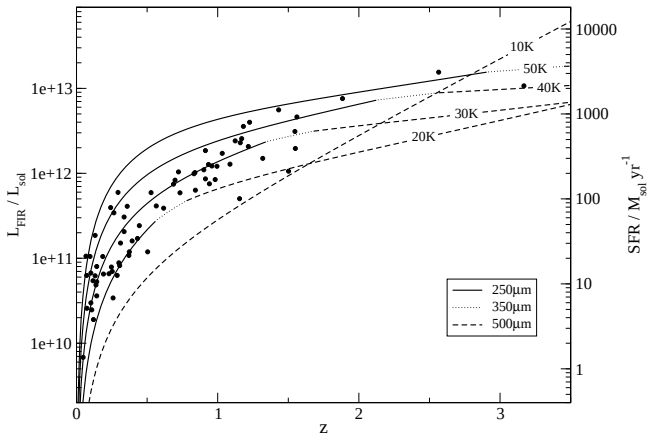

FIG. 8.— Correlation between total far-IR/submm luminosity, $L_{\rm FIR}$, and redshift for our robust sample of 74 sources. The right hand ordinate gives the star formation rate (SFR) in $M_\odot$/year estimated from the scaling: $\mathrm{SFR}/M_\odot\,\mathrm{yr}^{-1} = 2.0\times10^{-10} L_{\rm FIR}/L_\odot$ (Hughes et al. 1997). The different curves show, for a range of dust temperatures as labelled, the minimum $L_{\rm FIR}$ a source must have in order to be detected at 5σ in one of the three BLAST bands. The band in which this threshold occurs is indicated by the line style displayed in the legend. The 5σ detection limits used are those applicable to the BGS-Deep survey region (55, 45 and 30 mJy/beam at 250, 350 and 500 μm respectively).

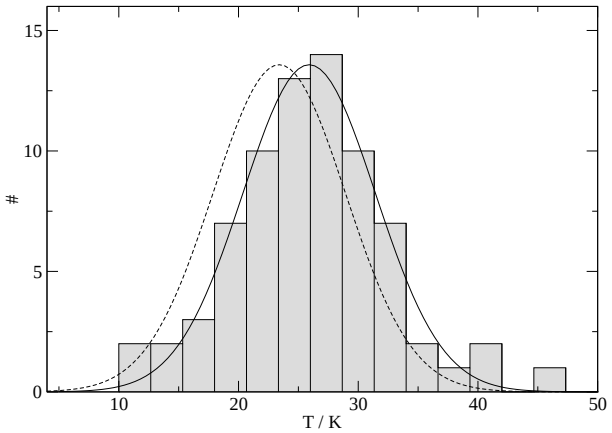

FIG. 9.— Histogram of dust temperatures for our robust sample of 74 sources (see text). The plotted best fit Gaussian (continuous line) has a 1σ width of 5.2 K and mean of 25.9 K. Repeating the analysis but changing β from 1.5 to 2.0 gives a very similar distribution with mean 23.4 K (dashed line).

fixed value of $\beta = 1.5$. The distribution is well approximated by a Gaussian of mean 26 K and 1σ width of 5 K. This spread in temperatures is comparable to the 1σ error on the mean of 4 K determined through error propagation. Fixing $\beta = 2$ instead gives a similar distribution but shifted to slightly lower temperatures with a mean of 23 K.

Comparing our dust temperatures with those derived for submm sources detected at 850 μm by SCUBA, we find that the BLAST sources are significantly cooler on average. The sample of 73 SCUBA sources of Chapman et al. (2005) has a median dust temperature of 36 ± 6 K, Kovacs et al. (2006) determined a median temperature of 35 ± 3 K for their sample of 15 sources while the sample of 25 SHADES galaxies studied by Coppin et al. (2008) was found to have a median temperature of 29 K (but with a large scatter of 18 K). As we discussed in Section 4.2, the SCUBA sources lie at

significantly higher redshifts on average, hence an obvious question is whether our sample of BLAST sources supports a trend for hotter sources at higher redshifts.

Figure 10 shows the rest-frame dust temperatures for the BLAST sources in our robust sample plotted against redshift. The scatter is large, but it is clear that hotter than average sources lie at higher redshifts. However, the selection effects discussed previously must be taken into consideration. The curves in Figure 10 are the sensitivity curves from Figure 8 transformed into the $T - z$ plane. For a given redshift, the curves in Figure 10 show that there is a dust temperature where the threshold in luminosity for detection is minimised. This is shown by the thin continuous line. Since lower luminosity sources are more common at a given redshift, this minimum threshold luminosity is where a population of sources with a uniform distribution of temperatures and dust masses would be expected to lie. Moving to colder or hotter temperatures away from this threshold at a fixed redshift requires a higher luminosity for detection. This is one of two dominant selection effects.

The second dominant selection effect arises from the fact that in reality, the dust mass distribution is far from uniform. Moving toward colder temperatures along a line of constant luminosity in Figure 10 requires the dust mass of a source to increase rapidly to stay within the survey sensitivity limits. For example, moving from $T = 30$ K to $T = 20$ K along the curve corresponding to $L_{\rm FIR} = 10^{12}\,L_\odot$ requires an increase in dust mass from $\sim 5 \times 10^6\,{\rm M}_\odot$ to $\sim 5 \times 10^7\,{\rm M}_\odot$ (assuming a dust mass opacity coefficient of $0.1{\rm m}^2/{\rm kg}$). Using the dust mass function of local submm galaxies determined by Vlahakis et al. (2005), there are ~ 10 times as many galaxies with a dust mass of $5 \times 10^6\,{\rm M}_\odot$ than with a dust mass of $5 \times 10^7\,{\rm M}_\odot$. This required dust mass at 20 K corresponds to the knee in the dust mass function, beyond which galaxies with more dust become vastly more rare. Repeating the estimate for 10 K results in an expected reduction in the number of galaxies by a factor of $\sim 10^6$. Along the higher luminosity sensitivity curves, the same principles apply but since dust mass is proportional to luminosity for a fixed temperature the knee of the dust mass function and therefore the sudden rarity of galaxies applies at warmer temperatures.

This strong selection effect pushes sources away from the minimum threshold luminosity plotted in Figure 10. The observed trend of increasing rest-frame dust temperature with redshift is therefore where the strength of both selection effects are approximately balanced. Both cause an observed increase in temperature with redshift, but the luminosity effect limits the upper detectable temperature and the dust mass effect limits the lower temperature.

In Figure 11, we plot the dust temperature of sources in our robust sample against luminosity. The straight line fit is $T = -12.9 + 3.4\,\log_{10}(L_{\rm FIR}/L_\odot)$. The increase in temperature at higher luminosity is a reflection of the trend discussed previously. This is consistent with a known positive correlation between intrinsic dust temperature and far-IR luminosity for luminous infrared galaxies in the local Universe (Chapman et al. 2003; Chapin et al. 2009). A more complete investigation will be discussed in forthcoming work (Chapin et al., in preparation).

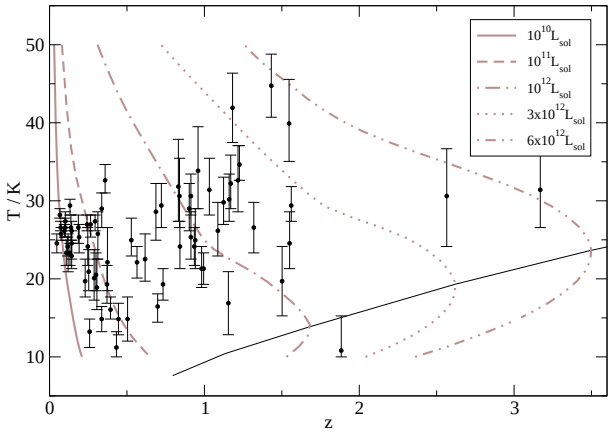

FIG. 10.— Correlation between rest-frame dust temperature, T, and redshift for our robust sample of 74 sources (see text). The curves show the sensitivity of the survey to redshift as a function of dust temperature for a source with a range of total far-IR/submm luminosities. The curves are determined by requiring a 5σ detection of the source in one of the three BLAST bands. The sensitivity limits used are those of BGS-Deep (55, 45 and 30 mJy/beam at 250, 350 and 500 μm respectively to 5σ). The thin continuous line in the lower part of the plot shows the dust temperature where the threshold in luminosity for detection is minimised for a given redshift. Sources do not lie along this threshold because it corresponds to high dust masses which are rare.

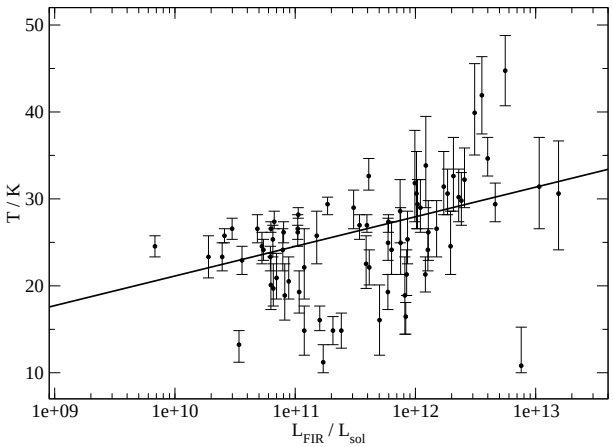

FIG. 11.— Correlation between dust temperature, T, and total far-IR/submm luminosity, $L_{\rm FIR}$, for our robust sample of 71 sources. The straight line fit is $T = -12.9 + 3.4\,\log_{10}(L_{\rm FIR}/L_\odot)$.

5. SUMMARY AND DISCUSSION

We have identified counterparts detected at 1.4GHz and/or 24 μm to 198 of the $350 \geq 5\sigma$ BLAST sources contained within the ~ 9 deg^2 of BGS-Wide and BGS-Deep centered on the CDFS. In the region within BGS-Deep covered by the deep 24 μm FIDEL catalog where we also have deep VLA data, the identification rate is 23/78 for the 24 μm sources and 29/78 for the radio sources. In the ~ 8 deg^2 surrounding the FIDEL region, the identification rate for 24 μm SWIRE sources is 131/268 compared with the rate of 74/220 using the Norris et al. radio catalog.

Of the identified counterparts, 114 have photometric redshifts previously estimated by COMBO-17 and/or Rowan-Robinson et al. (2008). Using these redshifts, we have fitted modified black body SEDs to the BLAST

fluxes measured at wavelengths 250, 350 and 500 μm and *Spitzer* fluxes at 70 and 160 μm. We have defined a robust sample of 74 sources whose SEDs fit the observed fluxes with $\chi^2 \leq N_{dof} + 2.71$ (rejecting the worse fit 10% assuming normal errors) and whose resulting best fit dust temperatures are not at the extremes of 10 K or 50 K of our uniform temperature prior.

The distribution of redshifts of our robust sample has a median of ~ 0.6 and an inter-quartile range of $0.2 - 1.0$. The dust temperatures are approximately normally distributed with a median temperature of $T \simeq 26 \pm 5$ K (for $\beta = 1.5$, or $T \simeq 23 \pm 5$ K for $\beta = 2$) and the distribution of bolometric far-IR/submm luminosity has a median of $4 \times 10^{11} L_{\odot}$.

Comparing the $\geq 5\sigma$ submm sources detected by BLAST with those detected by SCUBA at 850 μm, we find a stark contrast. It is clear from the redshift distributions alone that the BLAST sources in our robust sample are a significantly less distant population. The median redshift of submm sources detected to date in 850 μm SCUBA surveys lies somewhere between $z = 2 - 2.5$ (e.g., Chapman et al. 2005; Aretxaga et al. 2007; Younger et al. 2007). In comparison, 75% of the robust BLAST sources, for which we have identified counterparts in a similar manner to the SCUBA surveys (i.e., with a combination of radio and 24 μm data, the same used by Ivison et al. 2007, for example), lie at $z < 1$.

This significant difference can not be explained by our selection of robust sources. Within the subset of BLAST sources with identified counterparts, the robust sources form a uniform random sampling of the plane spanned by radio and 24 μm counterpart flux. In other words, we have not systematically failed to obtain redshifts for a more distant subset of identified BLAST sources where the radio and/or 24 μm flux would be expected to be lower on average. Therefore, we would not expect the redshift distribution of the full sample of 198 identified BLAST sources to extend to much greater redshifts. However, there remains the possibility that the remaining 153 BLAST sources without identified counterparts lie at higher redshifts on average. We have measured a decrease in the identification rate towards fainter BLAST fluxes which supports this hypothesis. Around a quarter of the 250 μm sources detected at $\geq 5\sigma$ remain unidentified compared to nearly two thirds of 500 μm sources.

We have compared our measured redshift distributions with predictions made by the galaxy evolution model of Lagache et al. (2004) and by our own model where we evolved the local 850 μm luminosity function with the empirical models of Rowan-Robinson et al. (2001). Considering sources detected at 250 μm, our own model implies that we have not failed to identify a significant number of 250 μm sources at higher redshift within the survey sensitivity limits. However, the Lagache model predicts that we may have failed to identify a small fraction ($\sim 10 - 15\%$) beyond $z \gtrsim 2$ which is compatible with our observed small decline in the identification rate at faint 250 μm fluxes. Conversely, at 500 μm, neither model implies a large enough fraction of high redshift sources to accommodate the strong decline in identification rate toward faint fluxes measured. This decline results in ~ 100 unidentified 500 μm sources. Even extending the models to include $\geq 3\sigma$ sources only shows a $\sim 25\%$ increase in the number of sources predicted at $z > 2$.

Considering all of the evidence presented (and bearing in mind that the models are not absolutely normalized), the most likely explanation is that the unidentified BLAST sources do indeed lie at higher redshifts than the identified subset on average, but that they also include a significant fraction of lower redshift sources. Failure to identify a low redshift source will occur if the counterpart is too faint, either to the extent that it is not detected or that it yields a value of P in the ID procedure that falls outside the threshold. To conclude our discussion of redshifts, although we cannot fully quantify the overlap of the redshift distribution of BLAST sources considered in this paper with that of the SCUBA population, we can place a strong upper limit. Under the extreme assumption that all 153 unidentified sources lie at higher redshift (say $z > 2$) than the 198 identified, the overlap with the SCUBA population is still just under 50%.

We have also found that the average dust temperature of the BLAST sources is clearly different to that of sources detected in the SCUBA surveys. The BLAST sources have a significantly cooler temperature distribution compared to the higher redshift 850 μm population. For example, Chapman et al. (2005) measured a median dust temperature of 36 ± 6 K. This is consistent with a trend observed in our sample of BLAST sources such that sources with higher dust temperatures are seen at higher redshifts. We have shown that this trend is the result of two strong selection effects.

This paper has addressed a small fraction of the analysis made possible by the multi-wavelength catalog of BLAST sources published herein and the identification of their radio and 24 μm counterparts. Further analysis will be conducted in forthcoming BLAST papers.

An immediate priority is to increase the number of source redshifts. We have very recently obtained spectroscopic redshifts with the multi-fiber spectrometer, AAOmega, on the Anglo-Australian telescope for > 100 of the BLAST sources (Eales et al. 2009). Preliminary results show very close agreement with the subset of sources in common that have previously derived photometric redshifts, although the spectroscopic sample extends the total number significantly. The multi-wavelength catalog (in combination with the *Spitzer* photometry at 70 and 160 μm) allows submm photometric redshifts to be estimated for those sources without counterparts. With a larger sample of redshifts, more stringent limits can be placed on galaxy evolution models and the redshift distributions they predict. These redshifts also enable investigation of the evolution of the submm luminosity function (Chapin et al., in preparation) and more rigorous investigation of the far-IR/radio correlation (Ivison et al., in preparation). Another possibility brought about by the spectra is measurement of equivalent line widths to provide a direct estimate of unobscured star formation rates. Combining spectra with optical/near-IR morphology will give new insight into the types of systems that BLAST, and hence Herschel (see below), is sensitive to. Determination of the dominant processes at play will greatly assist our understanding of the link between these systems and the local population of galaxies.

The photometry upon which the submm source prop-

erties derived in this paper have been based, the three BLAST bands at 250, 350 and 500 μm and the two *Spitzer* channels at 70 and 160 μm, is almost identical to what the Herschel Space Observatory is expected to deliver with SPIRE and PACS. Although the 9 deg^2 BLAST survey analyzed here represents a significant leap forward in terms of areal coverage of submm surveys, a subsequent leap is imminent with the anticipated several hundred square degree surveys to be conducted with Herschel.

APPENDIX

SUBMM SEDS

Figure 12 shows the best fit SEDs to the BLAST and *Splitzer* 70 and 160 μm data for the $\geq 5\sigma$ BLAST sources in the FIDEL region.

COUNTERPARTS OUTSIDE THE FIDEL REGION

Table 2 lists the radio and/or 24 μm counterparts to the BLAST sources outside the FIDEL region.

MULTI-WAVELENGTH BLAST CATALOG

Table 3 lists the 350 sources in the multi-wavelength catalog of $\geq 5\sigma$ BLAST sources in BGS-Wide and BGS-Deep centered on the CDFS. See Section 2.1 for a description of how this catalog was created. All sources are detected with a significance of $\geq 5\sigma$ in at least one of the bands.

Acknowledgments

We acknowledge the support of NASA through grant numbers NAG5-12785, NAG5- 13301, and NNGO-6GI11G, the NSF Office of Polar Programs, the Canadian Space Agency and the Natural Sciences and Engineering Research Council (NSERC) of Canada. This work is based in part on observations made with the Spitzer Space Telescope, which is operated by the Jet Propulsion Laboratory, California Institute of Technology under a contract with NASA. SD is supported by the UK Science and Technology Facilities Council (STFC). We thank Guilane Lagache for advice on implementation of her galaxy evolution models.

REFERENCES

Almaini, O., et al., 2003, MNRAS, 338, 303
Aretxaga, I., et al., 2007, MNRAS, 379, 1571
Barger, A. J., Cowie, L. L., Sanders, D. B., Fulton, E., Taniguchi, Y., Sato, Y., Kawara, K., & Okuda, H., 1998, Nature, 394, 248
Blain, A. W., Chapman, S. C., Smail, Ian, & Ivison, R., 2004, ApJ, 611, 725
Chapin, E., Hughes, D. H., & Aretxaga, I., 2009, MNRAS, 393, 653
Chapman, S. C., Helou, G., Lewis, G. F., & Dale, D. A., 2003, ApJ, 588, 186
Chapman, S. C., Blain, A.W., Smail, I., & Ivison, R.J., 2005, ApJ, 622, 772
Coppin, K., et al., 2006, MNRAS, 372, 1621
Coppin, K., et al., 2008, MNRAS, 384, 1597
Devlin, M. J., et al., 2004, SPIE, 5498, 42
Devlin, M. J., et al., 2009, Nature, 458, 737
Dickinson, M., et al., 'The Mass of Galaxies at Low and High Redshift', Proceedings of the European Southern Observatory and Universitäts-Sternwarte Mnchen Workshop, Held in Venice, Italy, 24-26 October 2001, ESO ASTROPHYSICS SYMPOSIA. ISBN 3-540-00205-7. Eds R. Bender and A. Renzini. Springer-Verlag, 2003, p. 324
Dickinson, M., et al., 2007, AAS, 211, 5216
Downes, A. J. B., Peacock, J. A., Savage, A., & Carrie, D. R., 1986, MNRAS, 218, 31
Dunne, L., Eales, S. A., Edmunds, M., Ivison, R., Alexander, P., Clements, D. L., 2000, MNRAS, 315, 115
Dunne, L., Eales, S. A., & Edmunds, M. G., 2003, MNRAS, 341, 589
Dye, S., Eales S., Ashby M., Huang J.-S., Egami E., Brodwin M., Lilly S., & Webb T., 2007, MNRAS, 375, 725
Dye, S., et al., 2008, MNRAS, 386, 1107
Eales, S. A., et al., 2009, ApJ, submitted
Fixsen, D.J., Dwek, E., Mather, J.C., Bennet, C.L., & Shafer, R.A., 1998, ApJ, 508, 123
Hauser, M. G. & Dwek E., 2001, ARA&A, 39, 249
Holland, W. S., et al., 1999, 303, 659
Hughes, D. H., Dunlop, J. S. & Rawlings, S., 1997, MNRAS, 289, 766
Hughes, D. H., et al., 1998, Nature, 394, 241
Ivison, R. J., et al., 2007, MNRAS, 380, 199
Kovacs, A., Chapman, S. C., Dowell, C. D., Blain, A. W., Ivison, R. J., Smail, I., Phillips, T. G., 2006, ApJ, 650, 592
Lagache, G., et al., 2004 ApJS, 154, 112
Lilly, S., Eales, S., Gear, W., Hammer, F., Le Fèvre, O., Crampton, D., Bond, J. R., & Dunne, L., 1999, ApJ, 518, 641
Lonsdale, C. J., et al., 2004, ApJS, 154, 54
Magnelli, B., Elbaz, D., Chary, R. R., Dickinson, M., Le Borgne, D., Frayer, D. T., & Willmer, C. N. A., 2009, A&A, 496, 57
Marsden, G., et al., 2009, ApJ, submitted, arXiv:0904.1205
Miller, N. A., Fomalont, E. B., Kellermann, K. I., Mainieri, V., Norman, C., Padovani, P., Rosati, P., & Tozzi, P., 2008, ApJS, 179, 71
Mortier, A., et al., 2005, MNRAS, 363, 563
Norris, R. P., et al., 2006, AJ, 132, 2409
Pascale, E., et al., 2008, AJ, 681, 400
Pascale, E., et al., 2009, ApJ, submitted, arXiv:0904.1206
Patanchon, G., et al., 2008, ApJ, 681, 708
Patanchon, G., et al., 2009, ApJ, submitted
Rowan-Robinson, M., 2001, Proceedings of the IAU Symposium 204, 'The Extragalactic Infrared Background and its Cosmological Implications', p.265, eds M.Harwit and M.G.Hauser
Rowan-Robinson, M., et al., 2008, 386, 697
Scott, S. E., et al., 2002, MNRAS, 331, 817
Smail, I., Ivison, R.J., & Blain, A.W., 1997, ApJ, 490, L5
Truch, M. D. P., et al., 2008, ApJ, 681, 415
Truch, M. D. P., et al., 2009, ApJ, submitted
Vlahakis, C., Dunne, L. & Eales, S. A., 2005, MNRAS 364, 1253
Wolf, C., et al., 2004, A&A, 421, 913
Younger, J. D., et al., 2007, ApJ, 671, 1531

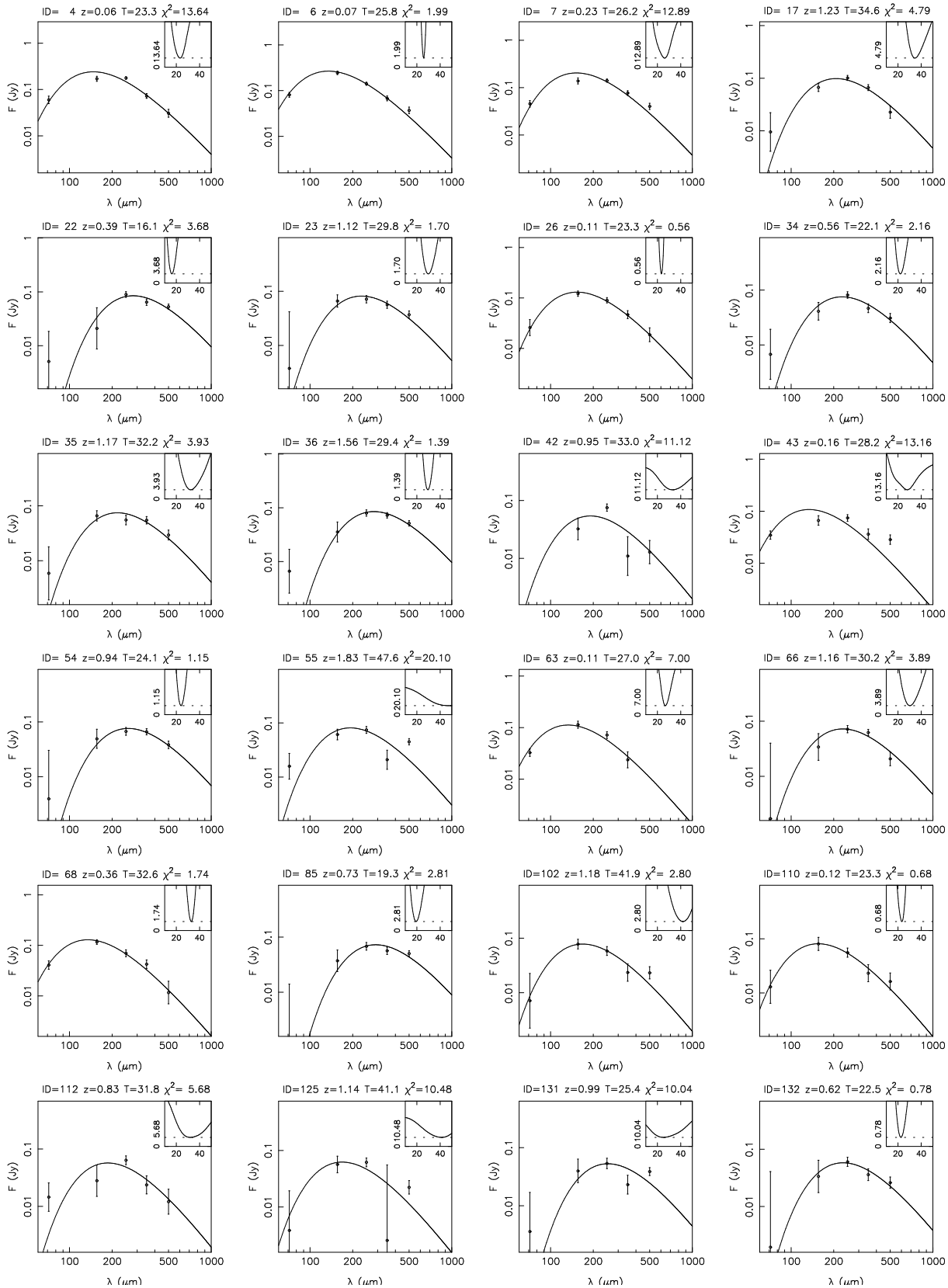

FIG. 12.— Best fit SEDs for $\geq 5\sigma$ BLAST sources in the FIDEL region. In the minimization, temperature is allowed to vary between 10 K and 50 K with a uniform prior, β is fixed at the value 2.0. Redshifts are fixed at the redshift of the optical counterpart. Where more than one redshift exists, that which gives the best fit to the BLAST data is taken. Inset plot in each panel shows χ^2 versus T.

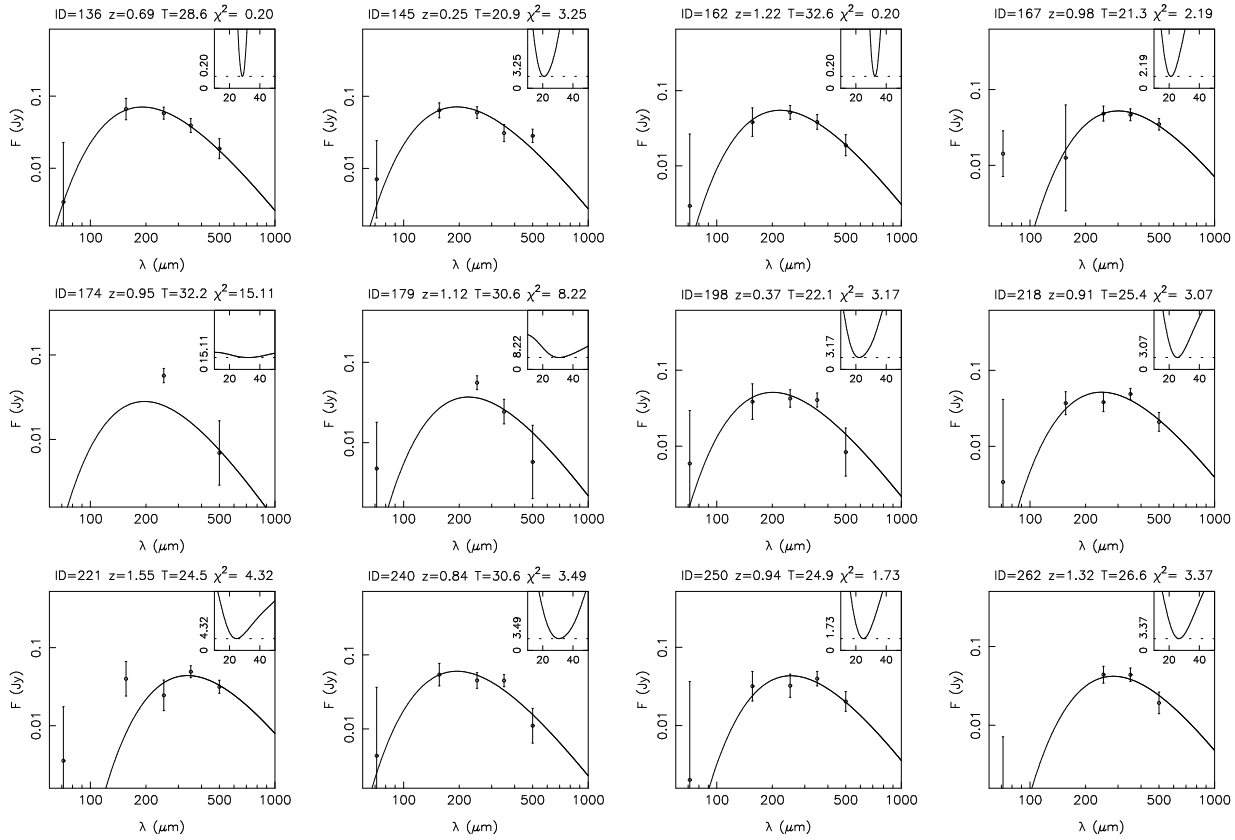

FIG. 12 *continued.*— Best fit SEDs for $\geq 5\sigma$ BLAST sources in the FIDEL region.

TABLE 2
Radio and 24 μm counterparts to the $\geq 5\sigma$ BLAST sources in the BLAST region outside the FIDEL region

ID	α (radio)	δ (radio)	$f_{\rm r}$	$P_{\rm r}$	$d_{\rm r}$	α (24 μm)	δ (24 μm)	f_{24}	P_{24}	d_{24}	$z_{\rm RR}$	z_{17}	T	$L_{\rm FIR}$	χ^2
1	52.33788	-28.13343	4.50	0.0005	3.3	52.33796	-28.13353	36.781	$< 10^{-4}$	2.9	-	-	-	-	-
2	52.48567	-28.77572	5.40	0.0004	3.0	-	-	-	-	-	-	-	-	-	-
3	51.92112	-28.38893	3.70	0.0015	5.8	51.92133	-28.38897	44.827	$< 10^{-4}$	5.4	0.07	-	$28.2^{+0.8}_{-0.4}$	10.6	3.80
5	52.88047	-27.47975	1.70	0.0014	4.4	52.88068	-27.47972	11.841	0.0002	4.1	-	-	-	-	-
8	53.95480	-27.82182	11.00	0.0005	4.6	53.95509	-27.82199	9.762	0.0004	5.3	-	-	-	-	-
9	-	-	-	-	-	52.31905	-27.65615	13.678	$< 10^{-4}$	3.2	0.07	-	$26.6^{+0.8}_{-0.4}$	6.28	4.46
10	-	-	-	-	-	52.20959	-26.61418	19.408	$< 10^{-4}$	4.2	-	-	-	-	-
11	53.60244	-27.75840	0.40	0.0013	2.7	53.60240	-27.75882	4.057	0.0009	4.1	-	-	-	-	-
12	52.28164	-28.68818	1.30	0.0014	3.9	52.28206	-28.68822	17.522	$< 10^{-4}$	3.8	0.09	-	$28.2^{+0.8}_{-0.4}$	10.5	7.73
13	52.45617	-28.84953	2.00	0.0028	7.2	52.45636	-28.84938	7.386	0.0009	6.7	0.10	-	$26.2^{+0.8}_{-0.8}$	10.5	1.04
15	53.42390	-28.12707	0.60	0.0033	5.2	53.42405	-28.12696	3.688	0.0020	5.7	0.27	-	$27.8^{+1.6}_{-1.2}$	22.2	17.0
16	52.74791	-28.16681	1.20	0.0032	6.3	52.74809	-28.16694	11.714	0.0004	7.0	0.10	-	$28.2^{+0.8}_{-0.8}$	7.12	7.10
18	52.84781	-27.94960	0.18	0.0142	11.1	52.84802	-27.94975	0.835	0.0415	10.3	-	0.91	$30.6^{+2.8}_{-2.4}$	185.	1.42
19	53.57372	-27.65888	0.70	0.0029	5.1	53.57382	-27.65890	7.192	0.0006	5.3	-	-	-	-	-
20	53.42222	-27.63578	0.79	0.0053	7.5	53.42229	-27.63586	8.676	0.0009	7.6	-	-	-	-	-
21	-	-	-	-	-	52.96558	-28.20779	2.551	0.0130	12.4	0.19	-	$26.6^{+1.6}_{-2.0}$	10.5	1.55
27	-	-	-	-	-	52.48787	-28.31118	9.878	0.0002	3.5	0.02	-	$25.4^{+0.8}_{-1.2}$	0.268	10.2
28	-	-	-	-	-	53.32528	-28.15234	1.033	0.0251	8.8	-	-	-	-	-
29	52.09459	-28.53271	1.30	0.0039	7.4	52.09475	-28.53271	15.632	0.0003	7.5	0.13	-	$29.4^{+0.8}_{-1.2}$	18.6	0.59
30	-	-	-	-	-	52.79799	-27.97185	1.018	0.0017	1.8	-	-	-	-	-
31	53.56034	-27.70594	0.50	0.0058	7.2	53.56038	-27.70619	6.526	0.0015	7.7	-	-	-	-	-
32	53.38408	-27.48811	0.30	0.0206	16.5	53.38424	-27.48819	4.418	0.0095	16.8	-	-	-	-	-
37	-	-	-	-	-	52.17858	-26.68290	13.441	0.0007	9.5	-	-	-	-	-
38	53.06646	-28.06318	0.14	0.0042	4.7	53.06629	-28.06340	0.883	0.0111	4.7	0.20	0.50	$23.3^{+2.4}_{-2.4}$	5.61	10.6
39	52.77753	-27.75455	2.00	0.0044	9.4	-	-	-	-	-	-	-	-	-	-
40	-	-	-	-	-	52.08769	-29.44216	12.497	0.0002	4.9	0.07	-	$25.8^{+1.2}_{-1.2}$	2.58	15.1
41	53.62771	-27.32085	1.40	0.0003	1.7	53.62807	-27.32084	25.644	$< 10^{-4}$	2.8	-	-	-	-	-
44	52.88014	-27.54425	0.11	0.0058	5.6	52.88030	-27.54424	0.475	0.0329	5.3	-	-	-	-	-
45	-	-	-	-	-	52.96289	-28.18947	0.898	0.0181	6.4	0.14	-	$22.9^{+1.6}_{-1.6}$	3.61	3.30
46	-	-	-	-	-	52.79430	-26.96136	4.734	0.0013	5.6	-	-	-	-	-
47	52.79519	-27.93269	0.06	0.0136	9.6	-	-	-	-	-	-	-	-	-	-
48	-	-	-	-	-	52.73177	-27.91680	0.718	0.0673	12.6	-	-	-	-	-
49	52.63681	-27.59523	0.50	0.0170	15.9	52.63707	-27.59490	4.694	0.0071	14.8	0.14	-	$26.2^{+1.2}_{-1.2}$	8.01	1.29
50	52.26844	-28.79759	0.90	0.0058	8.5	52.26871	-28.79818	3.039	0.0033	6.4	0.24	-	$27.0^{+1.2}_{-0.8}$	39.5	0.85
51	52.69279	-27.92153	0.50	0.0031	4.9	52.69297	-27.92202	3.178	0.0023	5.4	-	-	-	-	-
52	-	-	-	-	-	53.06131	-28.19199	0.374	0.0145	2.5	0.53	-	$24.9^{+2.8}_{-2.0}$	59.2	5.19
53	-	-	-	-	-	53.58170	-26.88803	3.059	0.0020	4.8	-	-	-	-	-
56	-	-	-	-	-	52.64380	-27.72466	1.252	0.0067	4.7	-	-	-	-	-
57	-	-	-	-	-	53.63655	-27.86255	0.977	0.0175	6.7	-	-	-	-	-
58	52.79956	-27.99783	0.08	0.0304	23.9	-	-	-	-	-	-	-	-	-	-
60	-	-	-	-	-	53.59264	-27.84540	1.913	0.0152	10.8	-	-	-	-	-
61	52.95233	-28.07629	0.21	0.0141	11.2	52.95238	-28.07612	0.289	0.1292	10.8	-	-	-	-	-
62	52.83376	-27.97194	0.07	0.0109	8.2	-	-	-	-	-	0.72	0.90	$29.4^{+2.8}_{-2.8}$	104.	1.60
64	53.16545	-28.05319	0.13	0.0060	5.8	53.16539	-28.05291	0.353	0.0565	6.0	-	-	-	-	-
65	-	-	-	-	-	52.57593	-27.91682	3.977	0.0001	1.3	0.05	-	$24.5^{+1.2}_{-1.2}$	0.682	4.13
69	-	-	-	-	-	52.97797	-28.17660	1.915	0.0305	16.9	0.31	-	$25.8^{+2.8}_{-3.2}$	15.1	2.00
70	-	-	-	-	-	52.79579	-28.80925	3.109	0.0089	11.6	0.12	-	$24.1^{+1.2}_{-1.2}$	5.44	3.29
71	52.91907	-27.49373	0.30	0.0066	6.9	52.91949	-27.49422	8.273	0.0011	8.4	-	-	-	-	-
72	52.83482	-27.56291	0.08	0.0041	4.3	52.83467	-27.56283	2.402	0.0018	3.7	0.19	-	$25.4^{+1.6}_{-2.0}$	6.52	3.56
73	52.99224	-27.58953	0.09	0.0085	7.2	52.99228	-27.58941	0.709	0.0288	6.9	1.00	0.22	$21.3^{+2.0}_{-2.0}$	121.	3.99
75	52.81060	-27.65189	0.11	0.0101	8.3	52.81075	-27.65190	1.501	0.0124	7.8	0.25	-	$24.1^{+2.4}_{-2.4}$	7.89	5.08
76	53.37103	-27.66588	0.13	0.0098	8.2	53.37101	-27.66590	0.470	0.0640	8.2	-	0.90	$29.0^{+3.2}_{-2.8}$	110.	3.89
77	53.07986	-27.52750	0.10	0.0088	7.4	53.07992	-27.52744	1.286	0.0146	7.6	0.23	-	$19.7^{+2.8}_{-2.0}$	6.58	5.17
78	-	-	-	-	-	53.50673	-27.79859	0.522	0.0342	5.9	-	-	-	-	-
80	52.99144	-28.70857	0.50	0.0176	16.3	-	-	-	-	-	-	-	-	-	-
83	-	-	-	-	-	54.14349	-28.70855	4.870	0.0035	10.1	0.29	-	$27.4^{+0.8}_{-1.2}$	59.6	1.68
84	53.32932	-28.24242	0.30	0.0031	4.3	53.32923	-28.24259	3.781	0.0008	3.6	0.10	-	$26.6^{+1.2}_{-1.2}$	2.99	3.87
86	53.69997	-28.50265	1.30	0.0014	3.9	53.70008	-28.50278	8.144	0.0002	3.5	0.07	-	$27.0^{+1.2}_{-1.2}$	2.64	11.6

Note. — (see Table 1 for counterparts within the FIDEL region). Reading from the left, columns are: radio co-ordinates, radio flux, f_r/mJy, probability of radio counterpart being a chance alignment, P_r, radio radial offset, $d_{\rm r}$/arcsec, 24 μm co-ordinates, 24 μm flux, f_{24}/mJy, probability of 24 μm counterpart being a chance alignment, P_{24}, 24 μm radial offset, d_{24}/arcsec, photometric redshift from Rowan-Robinson et al., $z_{\rm RR}$, COMBO-17 photometric redshift, z_{17}, best fit temperature, T/K, total far-IR/submm luminosity, $L_{\rm FIR}/(10^{10}L_{\odot})$ and χ^2 of the SED fit. Note that unlike Table 1, included here are counterparts with $0.05 < P \leq 0.1$. This results in an additional 29 counterparts at the expense of an expected extra two false counterparts. None of these additional counterparts are included in any of the analysis presented in this paper but are simply listed here for reference.

TABLE 2
continued – Radio and 24 μm counterparts to the $\geq 5\sigma$ BLAST sources outside the FIDEL region

ID	α (radio)	δ (radio)	f_r	P_r	d_r	α (24 μm)	δ (24 μm)	f_{24}	P_{24}	d_{24}	z_{RR}	z_{17}	T	L_{FIR}	χ^2
87	-	-	-	-	-	51.94289	-26.96452	4.102	0.0048	10.4	-	-	-	-	-
88	-	-	-	-	-	54.15564	-28.68730	11.775	0.0007	8.7	-	-	-	-	-
90	52.07532	-27.71906	1.50	0.0016	4.5	52.07560	-27.71935	5.607	0.0003	3.2	-	-	-	-	-
92	53.17420	-28.09792	0.30	0.0081	8.0	53.17420	-28.09762	0.827	0.0330	8.7	0.30	-	$20.5^{+2.8}_{-2.0}$	8.84	3.26
93	-	-	-	-	-	53.53340	-27.59049	0.830	0.0523	11.9	-	-	-	-	-
94	53.46999	-27.72898	0.20	0.0284	22.4	53.46997	-27.72978	1.702	0.0476	20.7	-	-	-	-	-
95	-	-	-	-	-	53.42970	-27.15331	6.743	0.0008	6.1	-	-	-	-	-
96	53.40470	-27.48562	0.30	0.0173	14.1	53.40502	-27.48516	3.293	0.0098	13.1	-	-	-	-	-
97	53.31762	-28.03985	0.07	0.0198	13.1	53.31769	-28.03985	0.600	0.0870	12.9	-	0.37	$19.3^{+2.4}_{-2.4}$	10.8	4.11
98	-	-	-	-	-	53.05950	-27.51728	0.509	0.0630	8.7	-	-	-	-	-
99	-	-	-	-	-	53.19616	-27.11917	4.900	0.0023	7.9	-	-	-	-	-
100	-	-	-	-	-	53.01636	-28.17114	0.327	0.0333	4.1	1.43	-	$44.7^{+4.0}_{-4.0}$	558.	1.18
101	-	-	-	-	-	52.86677	-28.16924	0.329	0.0806	7.5	-	-	-	-	-
103	-	-	-	-	-	51.78465	-27.09038	5.473	0.0032	10.3	-	-	-	-	-
106	-	-	-	-	-	51.76851	-28.12049	3.289	$< 10^{-4}$	0.9	-	-	-	-	-
109	-	-	-	-	-	53.53403	-27.90217	1.203	0.0177	8.1	-	-	-	-	-
113	53.45440	-27.64381	7.40	0.0093	24.0	-	-	-	-	-	-	-	-	-	-
115	52.86134	-28.08199	0.08	0.0300	22.7	-	-	-	-	-	-	-	-	-	-
118	53.15833	-27.53333	0.10	0.0135	10.2	53.15866	-27.53345	0.429	0.0929	10.0	-	-	-	-	-
119	-	-	-	-	-	54.03130	-27.38652	3.197	0.0070	10.4	-	-	-	-	-
120	-	-	-	-	-	51.76878	-28.49448	1.216	0.0494	16.0	-	-	-	-	-
122	52.60704	-27.83831	0.30	0.0026	3.8	52.60728	-27.83817	3.655	0.0008	3.7	0.14	-	$26.6^{+1.6}_{-1.6}$	4.85	5.09
123	-	-	-	-	-	52.80170	-26.95459	0.771	0.0009	1.0	-	-	-	-	-
126	-	-	-	-	-	53.05272	-28.54705	0.854	0.0379	9.8	0.56	-	$20.1^{+2.8}_{-2.4}$	47.1	8.21
127	-	-	-	-	-	53.10425	-29.28513	2.659	0.0009	2.9	0.13	-	$23.3^{+1.2}_{-1.6}$	6.22	3.09
128	-	-	-	-	-	52.75566	-27.88870	0.993	0.0480	13.1	0.96	-	$33.8^{+5.7}_{-4.8}$	122.	4.59
129	-	-	-	-	-	53.11398	-28.69950	3.275	0.0223	21.5	0.31	-	$29.0^{+1.6}_{-1.6}$	34.6	6.70
130	-	-	-	-	-	53.76858	-27.67370	0.626	0.0477	8.7	0.47	-	$21.7^{+4.8}_{-3.2}$	26.5	14.9
134	-	-	-	-	-	52.05436	-27.08062	6.204	0.0019	8.7	-	-	-	-	-
135	-	-	-	-	-	52.89175	-28.40077	3.010	0.0207	19.0	0.31	-	$29.0^{+2.0}_{-2.0}$	28.6	7.10
137	52.08969	-28.13662	1.10	0.0056	8.7	52.08987	-28.13661	6.388	0.0017	8.2	0.16	-	$27.8^{+1.2}_{-1.6}$	10.9	6.87
138	-	-	-	-	-	53.45399	-27.83728	0.477	0.0208	3.9	-	-	-	-	-
139	-	-	-	-	-	54.10876	-27.15997	10.366	0.0002	3.7	-	-	-	-	-
140	-	-	-	-	-	51.69027	-28.84995	0.708	0.0796	14.0	-	-	-	-	-
143	52.95023	-28.16929	0.20	0.0166	12.8	52.95030	-28.16876	2.387	0.0116	11.0	0.34	-	$29.0^{+2.0}_{-2.4}$	30.6	5.53
146	-	-	-	-	-	52.50169	-27.89651	2.905	0.0003	1.6	0.14	-	$24.5^{+1.6}_{-2.0}$	5.29	4.67
147	-	-	-	-	-	52.79279	-27.71546	0.565	0.0420	7.3	-	-	-	-	-
148	-	-	-	-	-	52.76799	-27.83581	0.463	0.0612	7.8	-	-	-	-	-
149	-	-	-	-	-	54.05851	-28.18294	3.236	0.0190	19.4	0.31	-	$27.4^{+2.8}_{-3.2}$	30.7	6.88
152	-	-	-	-	-	54.20443	-27.32740	4.858	0.0059	13.6	-	-	-	-	-
153	-	-	-	-	-	52.81561	-26.57759	1.055	0.0607	16.2	-	-	-	-	-
154	-	-	-	-	-	53.92210	-28.92295	3.853	0.0012	4.7	0.22	-	$28.6^{+1.6}_{-2.0}$	14.0	9.59
155	52.37314	-28.70542	1.50	0.0010	3.4	52.37320	-28.70511	8.731	0.0003	4.5	0.10	-	$27.4^{+1.2}_{-0.8}$	6.70	5.31
157	-	-	-	-	-	54.03839	-28.16214	2.994	0.0002	1.4	0.24	-	$27.0^{+1.6}_{-1.6}$	23.3	6.58
158	53.28065	-28.23637	0.30	0.0016	2.9	53.28098	-28.23623	3.994	0.0009	4.0	0.04	-	$27.0^{+1.6}_{-1.2}$	0.316	13.8
160	-	-	-	-	-	52.18251	-27.73569	0.459	0.0458	6.4	-	-	-	-	-
163	52.80927	-27.57008	0.08	0.0091	7.4	52.80905	-27.57013	0.734	0.0344	8.1	0.31	-	$18.9^{+3.6}_{-2.8}$	8.19	5.39
165	-	-	-	-	-	54.02465	-29.57020	1.738	0.0333	16.6	0.29	-	$31.0^{+4.8}_{-4.0}$	12.2	13.6
166	-	-	-	-	-	52.72938	-29.57429	4.336	0.0085	15.3	0.26	-	$27.0^{+1.2}_{-1.6}$	34.3	0.94
168	52.79785	-27.88311	0.14	0.0183	13.3	52.79799	-27.88293	2.823	0.0137	13.9	0.89	-	$50.0^{+0.0}_{-5.7}$	228.	6.82
169	-	-	-	-	-	53.14828	-28.10735	0.316	0.0150	2.4	1.55	-	$39.9^{+5.7}_{-4.8}$	311.	4.88
170	-	-	-	-	-	52.66032	-27.96378	1.433	0.0623	21.6	0.34	-	$24.5^{+4.0}_{-4.4}$	13.1	3.86
173	-	-	-	-	-	52.88347	-28.21739	0.269	0.0622	6.0	-	-	-	-	-
175	-	-	-	-	-	54.08544	-27.40627	11.236	0.0025	16.1	-	-	-	-	-
178	-	-	-	-	-	54.00227	-26.84850	0.680	0.0389	8.1	-	-	-	-	-
180	-	-	-	-	-	53.27217	-27.33042	0.531	0.0598	8.8	-	-	-	-	-
183	-	-	-	-	-	53.18489	-28.18372	1.193	0.0292	10.9	0.29	-	$20.1^{+3.6}_{-2.8}$	6.28	4.26
184	-	-	-	-	-	53.45900	-27.58877	0.275	0.0357	4.1	-	-	-	-	-
185	-	-	-	-	-	53.60793	-27.75361	1.841	0.0232	13.7	-	-	-	-	-
188	52.79504	-27.93130	0.14	0.0148	11.3	52.79525	-27.93162	1.792	0.0181	11.4	0.31	-	$23.3^{+2.8}_{-2.4}$	16.5	12.8
196	53.05087	-28.08790	0.07	0.0066	5.8	53.05111	-28.08795	0.280	0.0697	6.6	-	-	-	-	-
197	-	-	-	-	-	53.39648	-27.54589	0.850	0.0067	3.3	-	-	-	-	-
200	53.67066	-27.94234	0.40	0.0105	10.3	53.67042	-27.94180	3.390	0.0053	9.3	0.13	-	$26.6^{+2.0}_{-2.0}$	4.30	9.88
202	-	-	-	-	-	51.92740	-28.31520	1.055	0.0677	17.6	-	-	-	-	-

TABLE 2
continued – Radio and 24 μm counterparts to the $\geq 5\sigma$ BLAST sources outside the FIDEL region

ID	α (radio)	δ (radio)	$f_{\rm r}$	$P_{\rm r}$	$d_{\rm r}$	α (24 μm)	δ (24 μm)	f_{24}	P_{24}	d_{24}	$z_{\rm RR}$	z_{17}	T	$L_{\rm FIR}$	χ^2
203	53.87595	-28.18568	0.80	0.0136	15.1	53.87598	-28.18580	0.376	0.1716	15.6	-	-	-	-	-
204	53.40178	-27.73207	0.22	0.0031	4.0	53.40199	-27.73190	0.480	0.0286	4.8	-	1.09	$26.2^{+3.6}_{-3.2}$	128.	3.02
205	-	-	-	-	-	51.80349	-28.85086	1.303	0.0063	4.6	-	-	-	-	-
207	53.47462	-27.93015	0.30	0.0070	7.2	53.47474	-27.93006	1.199	0.0161	7.5	-	-	-	-	-
208	-	-	-	-	-	52.56557	-27.66277	0.533	0.0354	6.2	-	-	-	-	-
210	53.39663	-27.80555	0.06	0.0105	7.8	53.39699	-27.80564	0.645	0.0371	7.5	-	1.16	$27.8^{+4.4}_{-4.0}$	105.	12.4
212	-	-	-	-	-	52.86584	-28.17471	0.932	0.0041	2.7	0.99	-	$37.5^{+3.6}_{-4.0}$	302.	6.60
213	53.51498	-27.65649	0.20	0.0187	14.2	53.51506	-27.65668	0.526	0.1182	14.8	-	-	-	-	-
219	-	-	-	-	-	52.95915	-27.00111	0.782	0.0126	4.5	-	-	-	-	-
220	-	-	-	-	-	53.66620	-27.81678	0.659	0.0718	12.2	-	-	-	-	-
222	-	-	-	-	-	51.97130	-28.67426	1.245	0.0051	4.0	1.13	-	$29.0^{+3.2}_{-2.4}$	446.	8.41
223	53.59818	-27.74068	0.50	0.0186	17.1	-	-	-	-	-	-	-	-	-	-
225	-	-	-	-	-	52.84398	-27.88026	20.639	0.0009	17.2	-	-	-	-	-
226	-	-	-	-	-	54.34546	-27.67242	1.093	0.0138	6.3	0.44	-	$14.8^{+2.0}_{-2.0}$	24.2	5.50
231	53.54147	-27.87033	2.40	$< 10^{-4}$	0.9	53.54124	-27.86994	1.023	0.0031	2.5	-	-	-	-	-
232	-	-	-	-	-	53.05288	-27.43903	0.380	0.0443	5.3	-	-	-	-	-
236	53.39511	-27.88722	0.06	0.0306	23.8	-	-	-	-	-	-	1.50	$18.9^{+4.4}_{-4.4}$	81.7	1.00
238	-	-	-	-	-	52.06044	-28.98913	0.613	0.0769	11.9	0.44	-	$16.1^{+1.6}_{-1.6}$	42.4	0.74
239	-	-	-	-	-	52.83408	-27.82483	0.462	0.0270	4.5	0.97	0.84	$24.1^{+3.2}_{-2.8}$	63.3	2.71
245	-	-	-	-	-	51.96693	-29.15310	0.833	0.0221	6.8	0.34	-	$14.8^{+1.6}_{-1.6}$	20.6	1.30
246	-	-	-	-	-	52.72465	-27.95224	0.446	0.0283	4.5	-	-	-	-	-
248	-	-	-	-	-	53.44989	-27.24417	0.839	0.0909	18.0	-	-	-	-	-
252	-	-	-	-	-	53.94390	-29.16091	0.638	0.0808	12.9	0.32	-	$14.8^{+1.6}_{-1.6}$	13.5	3.99
253	-	-	-	-	-	51.86079	-29.32844	2.892	0.0027	5.4	-	-	-	-	-
254	-	-	-	-	-	52.91843	-27.51704	0.649	0.0567	10.1	-	-	-	-	-
255	52.84097	-27.85639	0.09	0.0098	7.9	52.84098	-27.85658	4.784	0.0020	7.3	1.03	1.34	$31.4^{+4.0}_{-3.2}$	172.	2.07
257	-	-	-	-	-	51.46241	-28.82178	0.516	0.0038	1.5	-	-	-	-	-
259	-	-	-	-	-	52.77208	-28.10434	3.131	0.0215	20.2	0.31	-	$30.2^{+2.8}_{-3.2}$	19.2	13.2
261	-	-	-	-	-	53.27457	-27.47684	1.288	0.0184	8.8	-	-	-	-	-
264	-	-	-	-	-	53.27784	-27.24149	0.385	0.0861	8.6	-	-	-	-	-
266	53.43335	-27.85256	0.06	0.0294	20.6	-	-	-	-	-	-	-	-	-	-
270	-	-	-	-	-	53.21302	-27.56991	0.398	0.0615	6.9	-	1.08	$33.8^{+2.8}_{-2.4}$	466.	9.72
274	52.71999	-27.91641	3.20	0.0078	16.0	-	-	-	-	-	0.89	-	$14.8^{+3.2}_{-2.8}$	50.9	10.2
275	-	-	-	-	-	52.95832	-28.16156	0.404	0.0405	5.2	1.46	-	$20.9^{+3.2}_{-2.8}$	188.	10.3
277	53.23040	-27.55273	0.08	0.0208	14.2	-	-	-	-	-	-	-	-	-	-
280	-	-	-	-	-	53.46829	-27.55235	0.497	0.0927	11.4	-	-	-	-	-
288	-	-	-	-	-	53.78062	-27.88157	0.726	0.0703	13.1	0.54	-	$17.7^{+1.6}_{-2.0}$	44.8	0.92
289	52.75508	-27.66077	0.20	0.0187	14.1	-	-	-	-	-	0.26	-	$13.2^{+1.6}_{-2.0}$	3.41	0.15
294	53.35498	-27.57369	0.06	0.0106	8.0	53.35495	-27.57305	0.481	0.0824	10.1	-	0.50	$14.8^{+2.8}_{-2.8}$	11.9	3.05
302	53.97283	-27.91971	1.00	0.0129	15.4	-	-	-	-	-	1.88	-	$10.8^{+4.4}_{-0.8}$	758.	4.86
303	52.84258	-27.96543	0.10	0.0151	11.1	52.84276	-27.96554	0.525	0.0845	11.2	0.19	0.60	$26.6^{+4.4}_{-3.6}$	49.4	12.1
304	53.13210	-28.07667	0.10	0.0020	2.9	-	-	-	-	-	-	-	-	-	-
307	-	-	-	-	-	53.04573	-27.09132	0.527	0.0532	8.0	-	-	-	-	-
309	-	-	-	-	-	52.80434	-27.50111	0.596	0.0949	13.7	-	-	-	-	-
311	-	-	-	-	-	52.57364	-28.50466	0.890	0.0090	4.2	2.57	-	$30.6^{+6.1}_{-6.5}$	1550.	2.65
318	-	-	-	-	-	53.04041	-28.12135	0.421	0.0725	8.1	0.75	-	$12.8^{+2.0}_{-2.0}$	20.8	3.25
319	-	-	-	-	-	52.64954	-27.62388	0.481	0.0649	8.5	-	-	-	-	-
320	-	-	-	-	-	51.74249	-29.27044	1.382	0.0517	18.4	-	-	-	-	-
322	53.34598	-28.05703	0.07	0.0261	17.7	-	-	-	-	-	-	1.15	$16.1^{+4.0}_{-4.0}$	50.3	1.17
323	-	-	-	-	-	53.98524	-28.59187	1.725	0.0420	19.2	0.28	-	$27.8^{+2.8}_{-3.6}$	15.7	11.7
329	53.39012	-28.23444	2.30	0.0148	23.1	-	-	-	-	-	3.17	-	$31.4^{+5.7}_{-4.8}$	1067.	2.47
332	-	-	-	-	-	52.66361	-27.79376	0.982	0.0321	9.9	-	-	-	-	-
333	-	-	-	-	-	54.20814	-27.99234	0.420	0.0180	3.2	0.70	-	$16.5^{+1.6}_{-2.0}$	83.1	2.01
335	-	-	-	-	-	54.05066	-29.08868	1.403	0.0196	9.9	0.29	-	$18.5^{+2.4}_{-2.0}$	18.7	7.91
339	-	-	-	-	-	52.57649	-28.85588	0.446	0.0428	5.9	0.33	-	$19.3^{+2.8}_{-1.6}$	24.4	6.43
341	-	-	-	-	-	53.69046	-27.84443	0.774	0.0289	7.5	-	-	-	-	-
342	-	-	-	-	-	51.93830	-29.39774	3.057	0.0165	16.6	-	-	-	-	-
343	-	-	-	-	-	53.62629	-27.61929	0.359	0.0454	5.2	-	-	-	-	-
344	-	-	-	-	-	53.16118	-28.09707	0.402	0.0657	7.3	-	-	-	-	-
346	-	-	-	-	-	51.76260	-28.18012	0.623	0.0770	12.1	-	-	-	-	-
355	-	-	-	-	-	52.82410	-27.33796	1.265	0.0226	9.8	-	-	-	-	-
359	-	-	-	-	-	53.94254	-27.49272	0.720	0.0452	9.5	-	-	-	-	-
360	-	-	-	-	-	51.89937	-28.98942	5.216	0.0114	21.3	0.43	-	$11.2^{+2.0}_{-1.2}$	17.1	0.92
368	-	-	-	-	-	52.48499	-29.05382	0.919	0.0552	13.6	0.11	-	$16.1^{+5.3}_{-2.8}$	1.36	14.1
369	-	-	-	-	-	53.49599	-29.62169	0.395	0.0767	8.0	-	-	-	-	-
376	-	-	-	-	-	52.63121	-26.82185	0.498	0.0341	5.6	-	-	-	-	-

TABLE 3
THE MULTI-WAVELENGTH CATALOG OF $\geq 5\sigma$ BLAST SOURCES IN BGS-WIDE AND BGS-DEEP.

ID	BLAST ID	f_{250}/Jy	σ_{250}/Jy	f_{350}/Jy	σ_{350}/Jy	f_{500}/Jy	σ_{500}/Jy
1	BLAST J032921-280803	0.997	0.033	0.472	0.026	0.196	0.018
2	BLAST J032956-284631	1.056	0.038	0.536	0.029	0.227	0.021
3	BLAST J032741-282325	0.639	0.036	0.240	0.029	0.084	0.019
4	BLAST J033235-275530	0.177	0.011	0.075	0.009	0.034	0.006
5	BLAST J033131-272842	0.234	0.015	0.101	0.013	0.038	0.009
6	BLAST J033229-274415	0.157	0.011	0.079	0.008	0.043	0.006
7	BLAST J033250-273420	0.159	0.011	0.089	0.009	-	-
8	BLAST J033548-274920	0.478	0.039	0.198	0.030	0.114	0.021
9	BLAST J032916-273919	0.418	0.034	0.195	0.026	0.074	0.018
10	BLAST J032850-263654	0.490	0.041	0.225	0.032	0.120	0.022
11	BLAST J033424-274527	0.164	0.014	-	-	-	-
12	BLAST J032907-284121	0.417	0.037	0.214	0.029	0.065	0.020
13	BLAST J032950-285058	0.381	0.037	0.147	0.029	0.072	0.021
14	BLAST J033128-273920	0.105	0.011	0.079	0.009	-	-
15	BLAST J033341-280742	0.123	0.013	0.065	0.010	-	-
16	BLAST J033059-280955	0.207	0.022	0.086	0.016	-	-
17	BLAST J033249-275838	0.101	0.011	0.073	0.009	-	-
18	BLAST J033123-275707	0.096	0.011	0.062	0.009	-	-
19	BLAST J033417-273927	0.125	0.014	0.061	0.011	0.034	0.008
20	BLAST J033340-273811	0.098	0.011	0.071	0.009	0.029	0.006
21	BLAST J033152-281235	0.118	0.014	0.062	0.011	0.031	0.008
22	BLAST J033152-273929	0.093	0.011	0.066	0.009	0.054	0.006
23	BLAST J033258-274324	0.093	0.011	0.065	0.009	0.039	0.006
24	BLAST J033129-275720	0.092	0.011	0.055	0.009	0.049	0.006
25	BLAST J033319-275423	0.091	0.011	0.029	0.008	-	-
26	BLAST J033246-275743	0.090	0.011	0.047	0.009	0.020	0.006
27	BLAST J032956-281843	0.276	0.034	-	-	-	-
28	BLAST J033317-280901	0.095	0.012	0.073	0.009	0.055	0.006
29	BLAST J032822-283205	0.284	0.035	0.102	0.027	-	-
30	BLAST J033111-275820	0.093	0.012	0.063	0.009	0.034	0.007
31	BLAST J033414-274217	0.103	0.013	0.042	0.010	-	-
32	BLAST J033332-272900	0.111	0.014	-	-	-	-
33	BLAST J033107-274023	0.097	0.012	0.063	0.010	0.060	0.007
34	BLAST J033149-274335	0.087	0.011	0.053	0.009	-	-
35	BLAST J033217-275905	0.085	0.011	0.065	0.008	0.036	0.006
36	BLAST J033317-274606	0.083	0.011	0.074	0.008	0.052	0.006
37	BLAST J032842-264107	0.317	0.042	-	-	0.066	0.021
38	BLAST J033216-280350	0.082	0.011	0.049	0.009	-	-
39	BLAST J033106-274508	0.086	0.012	0.047	0.010	-	-
40	BLAST J032821-292636	0.303	0.041	-	-	-	-
41	BLAST J033430-271915	0.273	0.037	0.135	0.029	-	-
42	BLAST J033145-274635	0.080	0.011	-	-	-	-
43	BLAST J033308-274809	0.080	0.011	0.045	0.008	0.036	0.006
44	BLAST J033131-273235	0.092	0.013	0.086	0.010	0.058	0.007
45	BLAST J033150-281126	0.091	0.013	-	-	-	-
46	BLAST J033110-265744	0.291	0.041	0.113	0.032	-	-
47	BLAST J033111-275605	0.080	0.011	-	-	-	-
48	BLAST J033054-275457	0.089	0.013	0.057	0.010	-	-
49	BLAST J033032-273527	0.158	0.022	0.077	0.019	0.046	0.013
50	BLAST J032904-284759	0.260	0.037	0.137	0.029	0.061	0.020
51	BLAST J033046-275515	0.097	0.014	0.040	0.011	-	-
52	BLAST J033214-281133	0.083	0.012	0.069	0.009	0.035	0.007
53	BLAST J033419-265319	0.275	0.040	0.162	0.030	-	-
54	BLAST J033151-274428	0.074	0.011	0.066	0.009	0.038	0.006
55	BLAST J033129-275557	0.074	0.011	-	-	0.051	0.006
56	BLAST J033034-274325	0.110	0.016	-	-	0.031	0.009
57	BLAST J033432-275140	0.099	0.015	0.040	0.011	0.033	0.008
58	BLAST J033110-280011	0.080	0.012	0.044	0.010	0.036	0.007
59	BLAST J033218-275212	0.074	0.011	0.064	0.009	0.048	0.006
60	BLAST J033421-275033	0.088	0.013	0.031	0.010	-	-
61	BLAST J033148-280424	0.074	0.011	0.056	0.009	-	-
62	BLAST J033119-275822	0.074	0.011	0.040	0.009	-	-
63	BLAST J033316-275045	0.072	0.011	0.034	0.008	-	-
64	BLAST J033240-280310	0.073	0.011	0.062	0.008	0.034	0.006
65	BLAST J033018-275500	0.149	0.023	-	-	-	-
66	BLAST J033205-274648	0.072	0.011	0.063	0.008	0.022	0.006
67	BLAST J033145-274159	0.073	0.011	0.038	0.009	0.041	0.006
68	BLAST J033146-275732	0.072	0.011	0.044	0.008	-	-

NOTE. — Reading from left to right, columns are: Internal ID as used throughout this paper, official combined BLAST source ID then flux and 1σ flux error for 250, 350 and 500 μm. To make the list, a source must be detected at $\geq 5\sigma$ in at least one band. Note that the fluxes quoted here have not been de-boosted and that errors are purely instrumental, neglecting the effects of source confusion (see Section 3.3 for further discussion).

TABLE 3
continued – The multi-wavelength catalog of $\geq 5\sigma$ BLAST sources in BGS-Wide and BGS-Deep

ID	BLAST ID	f_{250}/Jy	σ_{250}/Jy	f_{350}/Jy	σ_{350}/Jy	f_{500}/Jy	σ_{500}/Jy
69	BLAST J033153-281036	0.078	0.012	-	-	-	-
70	BLAST J033111-284835	0.252	0.039	0.093	0.029	-	-
71	BLAST J033140-272937	0.086	0.013	0.074	0.011	-	-
72	BLAST J033120-273344	0.083	0.013	0.043	0.011	-	-
73	BLAST J033158-273519	0.071	0.011	0.058	0.009	0.057	0.006
74	BLAST J033237-273531	0.071	0.011	0.058	0.009	0.046	0.006
75	BLAST J033115-273905	0.076	0.012	-	-	-	-
76	BLAST J033328-273949	0.072	0.011	0.033	0.009	0.025	0.006
77	BLAST J033218-273138	0.071	0.011	-	-	0.023	0.006
78	BLAST J033401-274759	0.072	0.011	0.041	0.009	0.026	0.006
80	BLAST J033156-284241	0.230	0.036	0.082	0.027	-	-
81	BLAST J033350-274254	0.072	0.011	0.058	0.009	-	-
82	BLAST J033054-275025	0.078	0.012	0.078	0.010	0.035	0.007
83	BLAST J033633-284223	0.227	0.036	0.145	0.028	0.069	0.019
84	BLAST J033318-281436	0.103	0.017	-	-	-	-
85	BLAST J033153-274950	0.068	0.011	0.059	0.009	0.052	0.006
86	BLAST J033447-283013	0.220	0.036	0.128	0.027	0.074	0.019
87	BLAST J032746-265801	0.254	0.041	0.107	0.032	0.088	0.022
88	BLAST J033636-284115	0.223	0.036	-	-	-	-
89	BLAST J033152-275032	0.067	0.011	0.064	0.008	0.044	0.006
90	BLAST J032818-274311	0.235	0.038	0.189	0.028	-	-
91	BLAST J033348-273435	0.076	0.012	-	-	-	-
92	BLAST J033241-280557	0.068	0.011	0.037	0.009	-	-
93	BLAST J033408-273514	0.093	0.015	0.071	0.011	0.034	0.008
94	BLAST J033351-274357	0.069	0.011	-	-	0.043	0.006
95	BLAST J033343-270918	0.248	0.041	0.099	0.033	-	-
96	BLAST J033336-272854	0.090	0.015	0.050	0.011	-	-
97	BLAST J033317-280220	0.067	0.011	0.035	0.009	0.028	0.006
98	BLAST J033214-273053	0.069	0.011	0.048	0.009	-	-
99	BLAST J033247-270716	0.240	0.040	0.106	0.030	0.098	0.021
100	BLAST J033203-281015	0.069	0.011	0.031	0.009	0.021	0.006
101	BLAST J033127-281009	0.086	0.014	-	-	0.047	0.008
102	BLAST J033124-275207	0.066	0.011	-	-	0.031	0.006
103	BLAST J032707-270516	0.237	0.040	-	-	-	-
104	BLAST J033129-275913	0.066	0.011	0.049	0.009	0.053	0.006
105	BLAST J033235-274930	0.065	0.011	0.039	0.008	0.044	0.006
106	BLAST J032704-280713	0.230	0.039	-	-	0.066	0.020
107	BLAST J033243-273917	0.065	0.011	0.037	0.009	0.026	0.006
108	BLAST J033045-280219	0.100	0.017	-	-	-	-
109	BLAST J033408-275415	0.070	0.012	-	-	0.026	0.007
110	BLAST J033217-275054	0.064	0.011	-	-	-	-
111	BLAST J033736-290254	0.224	0.038	-	-	0.077	0.020
112	BLAST J033241-273818	0.064	0.011	-	-	-	-
113	BLAST J033347-273848	0.066	0.011	0.041	0.009	-	-
114	BLAST J033844-275532	0.217	0.038	0.091	0.029	0.070	0.021
115	BLAST J033128-280508	0.068	0.012	0.046	0.009	-	-
116	BLAST J033039-273652	0.109	0.019	-	-	-	-
117	BLAST J033135-273934	0.063	0.011	0.033	0.009	-	-
118	BLAST J033238-273151	0.064	0.011	0.055	0.009	0.033	0.006
119	BLAST J033606-272311	0.229	0.040	0.139	0.031	0.093	0.021
120	BLAST J032703-282950	0.205	0.036	0.135	0.027	0.117	0.020
122	BLAST J033025-275014	0.099	0.017	0.060	0.015	0.038	0.010
123	BLAST J033112-265716	0.230	0.041	0.113	0.032	-	-
125	BLAST J033229-273505	0.063	0.011	-	-	0.023	0.006
126	BLAST J033211-283251	0.202	0.036	0.094	0.028	-	-
127	BLAST J033224-291707	0.218	0.039	0.097	0.030	-	-
128	BLAST J033100-275310	0.068	0.012	-	-	-	-
129	BLAST J033225-284148	0.203	0.036	0.127	0.029	0.067	0.020
130	BLAST J033505-274027	0.206	0.037	-	-	-	-
131	BLAST J033200-273604	0.061	0.011	-	-	-	-
132	BLAST J033225-273818	0.062	0.011	0.040	0.009	0.031	0.006
134	BLAST J032813-270453	0.225	0.040	-	-	0.073	0.022
135	BLAST J033134-282344	0.207	0.037	-	-	0.070	0.019
136	BLAST J033228-273547	0.061	0.011	0.050	0.009	0.023	0.006
137	BLAST J032822-280809	0.206	0.037	0.102	0.029	-	-
138	BLAST J033348-275015	0.061	0.011	0.046	0.008	0.025	0.006
139	BLAST J033626-270939	0.224	0.041	0.111	0.031	0.067	0.021
140	BLAST J032644-285106	0.210	0.038	0.125	0.029	0.140	0.020
141	BLAST J033023-275041	0.101	0.018	0.060	0.015	0.042	0.011
143	BLAST J033148-280958	0.066	0.012	0.072	0.009	-	-
144	BLAST J033020-275553	0.115	0.021	-	-	-	-

TABLE 3
continued – The multi-wavelength catalog of $\geq 5\sigma$ BLAST sources in BGS-Wide and BGS-Deep

ID	BLAST ID	f_{250}/Jy	σ_{250}/Jy	f_{350}/Jy	σ_{350}/Jy	f_{500}/Jy	σ_{500}/Jy
145	BLAST J033211-275859	0.060	0.011	-	-	-	-
146	BLAST J033000-275347	0.153	0.028	-	-	-	-
147	BLAST J033110-274302	0.063	0.012	0.052	0.009	-	-
148	BLAST J033104-275001	0.062	0.011	0.045	0.009	-	-
149	BLAST J033612-281046	0.206	0.038	0.107	0.030	0.083	0.021
150	BLAST J033416-280216	0.081	0.015	0.043	0.011	-	-
151	BLAST J033109-280045	0.066	0.012	-	-	0.036	0.007
152	BLAST J033648-271936	0.205	0.038	0.116	0.029	0.064	0.021
153	BLAST J033116-263428	0.230	0.043	-	-	-	-
154	BLAST J033541-285524	0.210	0.039	-	-	-	-
155	BLAST J032929-284222	0.200	0.038	0.140	0.028	0.063	0.021
157	BLAST J033609-280942	0.208	0.039	0.111	0.030	0.084	0.021
158	BLAST J033307-281412	0.081	0.015	0.065	0.011	-	-
159	BLAST J033752-283714	0.192	0.036	-	-	0.091	0.019
160	BLAST J032843-274414	0.191	0.036	-	-	-	-
161	BLAST J033132-273759	0.059	0.011	0.036	0.009	-	-
162	BLAST J033154-274406	0.057	0.011	-	-	-	-
163	BLAST J033114-273412	0.070	0.013	-	-	-	-
164	BLAST J033220-275640	0.058	0.011	0.066	0.009	0.036	0.006
165	BLAST J033605-293357	0.210	0.040	-	-	-	-
166	BLAST J033053-293431	0.196	0.037	0.090	0.028	0.098	0.020
167	BLAST J033247-274221	0.057	0.011	0.054	0.008	0.036	0.006
168	BLAST J033110-275303	0.058	0.011	0.033	0.009	-	-
169	BLAST J033235-280626	0.057	0.011	0.030	0.009	-	-
170	BLAST J033039-275805	0.079	0.016	0.047	0.013	-	-
171	BLAST J033118-273454	0.065	0.013	0.050	0.010	-	-
172	BLAST J033356-274556	0.058	0.011	0.054	0.009	0.047	0.006
173	BLAST J033132-281257	0.088	0.017	0.092	0.013	0.068	0.010
174	BLAST J033229-273948	0.057	0.011	-	-	-	-
175	BLAST J033619-272415	0.202	0.040	0.117	0.030	-	-
176	BLAST J033312-280758	0.059	0.012	0.040	0.009	0.032	0.006
177	BLAST J033346-274214	0.057	0.011	0.048	0.009	0.052	0.006
178	BLAST J033600-265102	0.210	0.041	0.107	0.031	-	-
179	BLAST J033259-273536	0.056	0.011	0.027	0.009	-	-
180	BLAST J033304-271943	0.187	0.037	0.084	0.028	0.089	0.019
181	BLAST J032745-280446	0.193	0.038	0.141	0.029	0.067	0.020
182	BLAST J033221-274107	0.056	0.011	-	-	0.031	0.006
183	BLAST J033245-281104	0.059	0.012	-	-	-	-
184	BLAST J033350-273520	0.062	0.012	0.039	0.010	-	-
185	BLAST J033424-274514	-	-	0.122	0.010	0.097	0.008
186	BLAST J033229-274307	-	-	0.076	0.008	0.043	0.006
187	BLAST J033328-275659	0.054	0.011	0.071	0.009	0.052	0.006
188	BLAST J033111-275546	-	-	0.075	0.009	-	-
189	BLAST J033218-273113	-	-	0.070	0.009	-	-
190	BLAST J033207-275813	0.048	0.011	0.066	0.009	0.065	0.006
191	BLAST J033347-273435	-	-	0.072	0.010	-	-
192	BLAST J033318-274125	0.051	0.011	0.064	0.009	0.038	0.006
193	BLAST J033252-273755	0.047	0.011	0.064	0.009	0.040	0.006
195	BLAST J033333-275926	0.036	0.011	0.059	0.009	0.042	0.006
196	BLAST J033211-280514	0.036	0.011	0.057	0.009	0.029	0.006
197	BLAST J033335-273244	0.044	0.012	0.062	0.009	0.038	0.007
198	BLAST J033215-273930	0.044	0.011	0.056	0.009	-	-
200	BLAST J033440-275630	0.074	0.018	0.084	0.013	-	-
201	BLAST J033356-280314	0.052	0.013	0.062	0.009	0.049	0.007
202	BLAST J032742-281911	0.161	0.037	0.178	0.028	0.133	0.020
203	BLAST J033529-281053	0.128	0.038	0.188	0.030	0.076	0.021
204	BLAST J033336-274359	0.049	0.011	0.054	0.009	0.022	0.006
205	BLAST J032713-285101	0.190	0.038	0.174	0.028	-	-
206	BLAST J033210-275207	-	-	0.054	0.009	0.037	0.006
207	BLAST J033353-275555	0.049	0.011	0.054	0.009	0.026	0.006
208	BLAST J033015-273940	-	-	0.131	0.021	0.052	0.014
210	BLAST J033335-274827	0.039	0.011	0.052	0.008	-	-
211	BLAST J033335-281422	-	-	0.085	0.014	-	-
212	BLAST J033127-281027	-	-	0.070	0.012	0.047	0.008
213	BLAST J033402-273916	0.059	0.012	0.058	0.010	0.036	0.007
214	BLAST J033251-281037	0.049	0.011	0.054	0.009	0.052	0.006
216	BLAST J033311-272223	0.097	0.028	0.131	0.022	-	-
217	BLAST J033312-275609	0.045	0.011	0.051	0.009	0.048	0.006
218	BLAST J033141-275530	0.038	0.011	0.050	0.008	-	-
219	BLAST J033150-270007	0.195	0.043	0.184	0.032	0.088	0.022
220	BLAST J033440-274905	-	-	0.070	0.012	0.043	0.008

TABLE 3
continued – The multi-wavelength catalog of $\geq 5\sigma$ BLAST sources in BGS-Wide and BGS-Deep

ID	BLAST ID	f_{250}/Jy	σ_{250}/Jy	f_{350}/Jy	σ_{350}/Jy	f_{500}/Jy	σ_{500}/Jy
222	BLAST J032753-284023	-	-	0.168	0.029	-	-
223	BLAST J033423-274409	0.064	0.014	0.060	0.010	-	-
224	BLAST J033134-274628	-	-	0.049	0.009	0.021	0.006
225	BLAST J033123-275233	-	-	0.048	0.008	-	-
226	BLAST J033723-274021	-	-	0.163	0.029	-	-
227	BLAST J033134-280059	0.038	0.011	0.048	0.009	-	-
228	BLAST J033635-283558	0.126	0.036	0.154	0.028	0.104	0.019
229	BLAST J033102-274456	0.059	0.012	0.055	0.010	-	-
230	BLAST J033150-280557	0.055	0.011	0.049	0.009	0.039	0.006
231	BLAST J033409-275213	0.056	0.012	0.050	0.009	-	-
232	BLAST J033213-272619	-	-	0.067	0.012	0.038	0.008
233	BLAST J033110-274515	0.051	0.011	0.051	0.009	0.052	0.007
234	BLAST J033249-273109	-	-	0.048	0.009	0.022	0.006
235	BLAST J033302-275635	-	-	0.047	0.009	0.031	0.006
236	BLAST J033336-275328	0.036	0.011	0.047	0.009	0.032	0.006
237	BLAST J033135-275449	0.033	0.011	0.047	0.009	0.046	0.006
238	BLAST J032813-285930	0.143	0.041	0.174	0.032	0.124	0.022
239	BLAST J033120-274933	0.049	0.011	0.046	0.008	0.021	0.006
240	BLAST J033306-274415	0.050	0.011	0.046	0.009	-	-
241	BLAST J033417-280108	0.060	0.014	0.059	0.011	0.051	0.008
242	BLAST J033243-274728	0.040	0.011	0.045	0.008	-	-
244	BLAST J033732-275836	0.117	0.037	0.148	0.028	-	-
245	BLAST J032752-290904	0.124	0.040	0.163	0.031	0.103	0.021
246	BLAST J033053-275704	-	-	0.058	0.011	-	-
247	BLAST J033309-275124	0.051	0.011	0.045	0.008	0.036	0.006
248	BLAST J033346-271431	-	-	0.161	0.030	-	-
249	BLAST J032617-283344	0.123	0.036	0.146	0.028	0.069	0.019
250	BLAST J033138-274122	-	-	0.044	0.008	-	-
251	BLAST J033307-275831	-	-	0.045	0.009	0.021	0.006
252	BLAST J033545-290948	-	-	0.151	0.029	0.069	0.021
253	BLAST J032726-291936	0.160	0.039	0.157	0.030	0.105	0.021
254	BLAST J033141-273107	0.047	0.013	0.053	0.010	-	-
255	BLAST J033122-275130	0.053	0.011	0.044	0.008	0.031	0.006
256	BLAST J033452-280119	-	-	0.096	0.018	-	-
257	BLAST J032550-284919	0.139	0.038	0.147	0.028	-	-
258	BLAST J033321-275512	-	-	0.044	0.009	0.032	0.006
259	BLAST J033105-280634	0.063	0.015	0.064	0.012	0.058	0.009
260	BLAST J033314-272913	-	-	0.050	0.010	-	-
261	BLAST J033306-272831	0.061	0.013	0.051	0.010	-	-
262	BLAST J033242-275511	0.048	0.011	0.044	0.009	0.019	0.006
263	BLAST J032537-293422	0.122	0.040	0.155	0.030	0.096	0.021
264	BLAST J033306-271435	-	-	0.157	0.031	0.105	0.021
265	BLAST J033127-274430	-	-	0.043	0.009	-	-
266	BLAST J033342-275117	-	-	0.043	0.009	-	-
267	BLAST J033322-283356	-	-	0.146	0.029	-	-
268	BLAST J033231-281247	-	-	0.050	0.010	0.030	0.007
269	BLAST J032623-285456	-	-	0.147	0.029	0.082	0.020
270	BLAST J033251-273417	-	-	-	-	0.058	0.006
271	BLAST J033128-273942	-	-	-	-	0.055	0.006
272	BLAST J033217-273042	0.056	0.011	-	-	0.052	0.006
273	BLAST J033050-275529	0.062	0.013	-	-	0.062	0.008
274	BLAST J033053-275513	-	-	-	-	0.060	0.007
275	BLAST J033149-280936	-	-	-	-	0.052	0.006
276	BLAST J033347-273503	0.054	0.012	-	-	0.050	0.007
277	BLAST J033254-273308	0.038	0.011	-	-	0.043	0.006
278	BLAST J033149-280311	0.053	0.011	-	-	0.042	0.006
279	BLAST J033354-280720	-	-	-	-	0.053	0.008
280	BLAST J033351-273306	0.052	0.013	0.040	0.010	0.051	0.007
282	BLAST J033412-275210	-	-	-	-	0.045	0.007
283	BLAST J033045-274633	0.053	0.014	0.038	0.011	0.053	0.008
284	BLAST J033110-273702	-	-	0.042	0.010	0.047	0.007
287	BLAST J033256-280102	-	-	0.039	0.009	0.040	0.006
288	BLAST J033507-275242	0.104	0.034	0.101	0.021	0.090	0.014
289	BLAST J033102-273948	0.049	0.013	0.049	0.010	0.048	0.007
290	BLAST J033212-275601	-	-	0.029	0.008	0.039	0.006
291	BLAST J033118-272849	-	-	0.054	0.016	0.066	0.010
292	BLAST J033229-280358	-	-	-	-	0.039	0.006
293	BLAST J033215-275018	-	-	0.037	0.009	0.038	0.006
294	BLAST J033324-273432	-	-	0.037	0.009	0.039	0.006
296	BLAST J033244-281158	0.052	0.012	-	-	0.043	0.007

TABLE 3
continued – The multi-wavelength catalog of $\geq 5\sigma$ BLAST sources in BGS-Wide and BGS-Deep

ID	BLAST ID	f_{250}/Jy	σ_{250}/Jy	f_{350}/Jy	σ_{350}/Jy	f_{500}/Jy	σ_{500}/Jy
297	BLAST J033028-275625	0.084	0.019	0.071	0.015	0.065	0.010
299	BLAST J033336-275751	0.050	0.011	0.038	0.009	0.038	0.006
300	BLAST J033114-273556	-	-	-	-	0.046	0.007
301	BLAST J033128-273745	-	-	0.038	0.009	0.040	0.006
302	BLAST J033552-275511	-	-	-	-	0.130	0.021
303	BLAST J033121-275803	-	-	-	-	0.038	0.006
304	BLAST J033231-280437	0.049	0.011	0.037	0.009	0.037	0.006
306	BLAST J033154-284219	-	-	-	-	0.118	0.019
307	BLAST J033210-270531	-	-	-	-	0.128	0.021
309	BLAST J033113-273016	0.081	0.017	0.072	0.015	0.057	0.009
310	BLAST J033021-282344	-	-	0.100	0.028	0.117	0.020
311	BLAST J033017-283020	-	-	-	-	0.113	0.019
312	BLAST J033052-274206	0.060	0.013	0.041	0.011	0.045	0.008
313	BLAST J033336-272934	-	-	0.034	0.011	0.046	0.008
314	BLAST J033138-274853	-	-	0.037	0.008	0.035	0.006
316	BLAST J032840-270822	0.130	0.041	-	-	0.129	0.022
318	BLAST J033210-280711	-	-	0.041	0.009	0.035	0.006
319	BLAST J033036-273717	0.080	0.019	0.074	0.017	0.063	0.011
320	BLAST J032656-291615	0.150	0.037	0.088	0.029	0.111	0.019
321	BLAST J033423-273224	0.084	0.024	0.055	0.017	0.067	0.012
322	BLAST J033321-280333	-	-	-	-	0.035	0.006
323	BLAST J033557-283540	0.153	0.036	-	-	0.113	0.020
324	BLAST J033239-272942	0.035	0.011	-	-	0.036	0.006
325	BLAST J032950-280013	-	-	0.077	0.024	0.097	0.017
326	BLAST J033205-273043	-	-	0.033	0.009	0.037	0.007
327	BLAST J033358-275357	0.035	0.011	0.040	0.009	0.034	0.006
328	BLAST J033743-283135	-	-	-	-	0.105	0.019
329	BLAST J033332-281348	-	-	-	-	0.050	0.009
330	BLAST J033403-274321	0.042	0.012	0.041	0.009	0.037	0.007
332	BLAST J033038-274738	0.047	0.015	0.047	0.012	0.046	0.008
333	BLAST J033649-275932	0.141	0.036	0.112	0.028	0.107	0.019
335	BLAST J033611-290528	0.155	0.039	-	-	0.114	0.021
336	BLAST J033231-274541	0.037	0.011	-	-	0.032	0.006
337	BLAST J033154-275354	0.048	0.011	0.039	0.009	0.033	0.006
338	BLAST J033331-280944	-	-	-	-	0.038	0.007
339	BLAST J033018-285124	0.171	0.039	-	-	0.113	0.021
340	BLAST J033112-273333	-	-	-	-	0.044	0.008
341	BLAST J033445-275038	-	-	0.057	0.013	0.050	0.009
342	BLAST J032745-292408	-	-	0.136	0.032	0.123	0.023
343	BLAST J033430-273704	0.068	0.019	0.040	0.013	0.051	0.009
344	BLAST J033239-280553	-	-	-	-	0.032	0.006
345	BLAST J033723-275653	-	-	-	-	0.102	0.019
346	BLAST J032702-281055	0.155	0.037	-	-	0.109	0.021
347	BLAST J032857-281327	0.110	0.035	0.089	0.028	0.100	0.019
348	BLAST J033308-280545	-	-	-	-	0.032	0.006
349	BLAST J033720-265950	-	-	-	-	0.121	0.023
350	BLAST J033439-274212	-	-	0.046	0.013	0.049	0.009
351	BLAST J033125-264713	0.157	0.041	-	-	0.120	0.023
355	BLAST J033117-272006	-	-	0.133	0.028	0.107	0.021
356	BLAST J033200-283721	-	-	-	-	0.100	0.019
357	BLAST J033318-274926	-	-	-	-	0.031	0.006
358	BLAST J033356-273613	-	-	0.031	0.010	0.035	0.007
359	BLAST J033545-272937	-	-	0.105	0.029	0.105	0.020
360	BLAST J032735-285902	-	-	0.107	0.031	0.113	0.022
361	BLAST J033527-284233	-	-	-	-	0.105	0.020
362	BLAST J033445-280222	0.092	0.025	0.070	0.017	0.059	0.011
363	BLAST J033212-274258	0.043	0.011	0.030	0.009	0.031	0.006
365	BLAST J033453-282822	0.121	0.036	-	-	0.100	0.019
366	BLAST J033246-281629	-	-	0.060	0.014	0.052	0.010
367	BLAST J033049-291151	-	-	-	-	0.104	0.020
368	BLAST J032957-290321	0.135	0.039	-	-	0.105	0.021
369	BLAST J033359-293715	0.145	0.039	-	-	0.108	0.021
371	BLAST J033209-280118	-	-	0.028	0.008	0.030	0.006
372	BLAST J032702-284013	-	-	-	-	0.103	0.020
373	BLAST J033342-272413	0.128	0.026	-	-	0.070	0.014
374	BLAST J033252-275929	0.052	0.011	-	-	0.030	0.006
375	BLAST J032656-284912	-	-	-	-	0.101	0.020
376	BLAST J033031-264922	0.155	0.041	-	-	0.108	0.021
377	BLAST J032603-281109	-	-	-	-	0.098	0.019
378	BLAST J033143-274817	-	-	-	-	0.029	0.006